CFHTLenS: weak lensing calibrated scaling relations for low-mass clusters of galaxies

K. Kettula,[1,2]★ S. Giodini,[3] E. van Uitert,[4] H. Hoekstra,[3] A. Finoguenov,[1,5]
M. Lerchster,[1,5] T. Erben,[4] C. Heymans,[6] H. Hildebrandt,[4,7] T. D. Kitching,[8]
A. Mahdavi,[9] Y. Mellier,[10,11] L. Miller,[12] M. Mirkazemi,[5] L. Van Waerbeke,[7]
J. Coupon,[13,14] E. Egami,[15] L. Fu,[16] M. J. Hudson,[17,18] J. P. Kneib,[19,20] K. Kuijken,[3]
H. J. McCracken,[10,11] M. J. Pereira,[14] B. Rowe,[21,22] T. Schrabback,[3,4,23] M. Tanaka[24]
and M. Velander[3,10]

Affiliations are listed at the end of the paper

ABSTRACT

We present weak lensing and X-ray analysis of 12 low-mass clusters from the Canada–France–Hawaii Telescope Lensing Survey and *XMM*-CFHTLS surveys. We combine these systems with high-mass systems from Canadian Cluster Comparison Project and low-mass systems from Cosmic Evolution Survey to obtain a sample of 70 systems, spanning over two orders of magnitude in mass. We measure core-excised L_X–T_X, M–L_X and M–T_X scaling relations and include corrections for observational biases. By providing fully bias-corrected relations, we give the current limitations for L_X and T_X as cluster mass proxies. We demonstrate that T_X benefits from a significantly lower intrinsic scatter at fixed mass than L_X. By studying the residuals of the bias-corrected relations, we show for the first time using weak lensing masses that galaxy groups seem more luminous and warmer for their mass than clusters. This implies a steepening of the M–L_X and M–T_X relations at low masses. We verify the inferred steepening using a different high-mass sample from the literature and show that variance between samples is the dominant effect leading to discrepant scaling relations. We divide our sample into subsamples of merging and relaxed systems, and find that mergers may have enhanced scatter in lensing measurements, most likely due to stronger triaxiality and more substructure. For the L_X–T_X relation, which is unaffected by lensing measurements, we find the opposite trend in scatter. We also explore the effects of X-ray cross-calibration and find that *Chandra* calibration leads to flatter L_X–T_X and M–T_X relations than *XMM–Newton*.

Key words: gravitational lensing: weak – galaxies: clusters: general – cosmology: observations – dark matter – X-rays: galaxies: clusters.

1 INTRODUCTION

Precise knowledge of the total mass of galaxy clusters is a crucial ingredient in order to probe cosmology by means of cluster number counts. Cluster masses can be inferred by means of gravitational lensing, from the velocity dispersion of cluster galaxies assuming dynamical equilibrium, or from X-ray surface brightness and temperatures assuming hydrostatic equilibrium (HSE). However, these direct methods are observationally expensive, especially for low-mass systems and at high redshifts. Fortunately, cluster mass scales with observational properties such as X-ray luminosity and temperature. Therefore it is possible to calibrate robust and well-understood scaling relations between cluster mass and observables, in order to be able to study statistical samples of clusters as cosmological probes.

Both simulations and observations show that clusters are found in various dynamical states, with bulk motions and non-thermal pressure components present in the intracluster gas. These affect mass measurements relying on dynamical equilibrium or HSE. In particular, as indicated in both simulations (e.g. Nagai, Kravtsov & Vikhlinin 2007; Shaw et al. 2010; Rasia et al. 2012), observations (e.g. Mahdavi et al. 2008, 2013; Kettula et al. 2013b; Donahue et al. 2014; Israel et al. 2014, 2015; von der Linden et al. 2014b) and recent analytical work by Shi & Komatsu (2014), HSE mass estimates differ from the lensing mass. The trend in the above

★ E-mail: kimmo.kettula@iki.fi

studies is that HSE mass estimates underestimate the true mass by ~10–30 per cent. However, as shown by e.g. the recent systematic comparison of mass estimates by Sereno & Ettori (2014), there is significant disagreement between different mass estimates relying on the same method. Though cluster triaxiality and substructure may complicate the interpretation, gravitational lensing provides the most reliable way of determining the true cluster mass, as it requires no assumptions on the thermodynamics of the intracluster gas or the dynamical state of the cluster.

In the self-similar case which assumes pure gravitational heating, cluster observables and mass are related by power-laws (Kaiser 1986). However, the relative strength of baryonic physics increases at low masses. Analysis by e.g. Nagai et al. (2007), Giodini et al. (2010), McCarthy et al. (2010), Stanek et al. (2010), Fabjan et al. (2011), Le Brun et al. (2014), Planelles et al. (2014) and Pike et al. (2014) indicate that baryonic processes such as non-gravitational feedback from star formation and active galactic nuclei (AGN) activity are expected to bias scaling relations from the self-similar prediction. The above works also indicate that the deviations are expected to be stronger for groups and low-mass clusters than for high-mass clusters. Hydrodynamical simulations by Schaye et al. (2010) show that the gas removed by AGN activity in groups can also affect the large-scale structure out to several Mpc, potentially skewing cosmic shear measurements (Semboloni et al. 2011; van Daalen et al. 2011; Semboloni, Hoekstra & Schaye 2013; Kitching et al. 2014). Consequently, characterization of the effects of feedback at group and low-mass cluster level is of high interest for both cluster and cosmic shear studies.

Indeed, recent detailed observations of groups and low-mass clusters by e.g. Sun et al. (2009), Eckmiller, Hudson & Reiprich (2011) and Lovisari, Reiprich & Schellenberger (2015) have reported evidence pointing to the direction of such mass-dependent deviations from self-similar scaling (see also Giodini et al. 2013, and references therein). Even if a direct measurement of a break in the scaling relations is hard, relations fitted to groups tend have a larger intrinsic scatter than similar relations fitted to massive clusters. However, most previous studies rely on X-ray mass estimates based on HSE. The HSE condition is broken by the same feedback processes affecting the scaling relations, and HSE masses are thus likely strongly biased for these low-mass systems (Kettula et al. 2013b). Therefore mass measurements by means of gravitational lensing are instrumental at group and low-mass cluster scales.

In the weak lensing regime, the gravitational potential of the cluster distorts light emitted by a background galaxy, resulting in a modified source ellipticity, known as shear. As galaxies have an intrinsic ellipticity which is typically larger than the lensing induced shear but not aligned with relation to the cluster, the shear has to be averaged over a statistical sample of source galaxies in order to measure the weak lensing signal.

The scaling of weak lensing mass to X-ray observables at galaxy group levels has previously only been studied in the COSMOS field by Leauthaud et al. (2010) and Kettula et al. (2013b), and recently at low-mass cluster levels by Connor et al. (2014). In this work, we focus on studying the scaling of weak lensing mass to X-ray luminosity L_X and spectroscopic temperatures T_X for a sample of low-mass clusters, with a typical mass of ~10^{14} M$_\odot$. The studied systems are in the 'sweet spot', where they are massive enough to be studied with reasonable observational effort and, at the same time, non-gravitational processes still give a significant contribution to their energetics (see Fig. 1). This is quantified in Fig. 1, which shows the ratio of non-gravitational mechanical energy released by AGNs to the gravitational binding energy of the intracluster gas
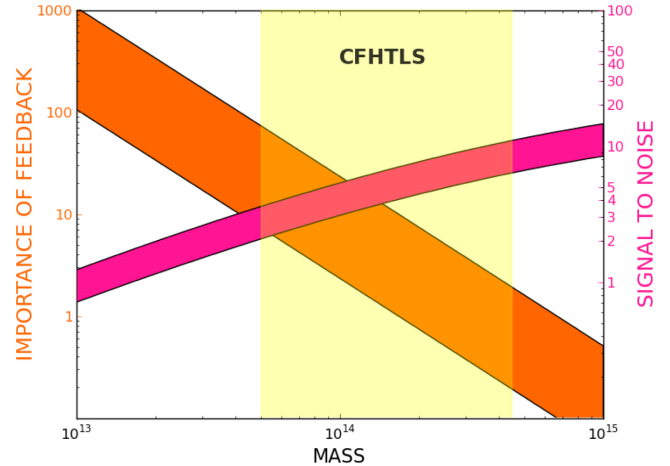

Figure 1. The importance of feedback (in orange) increases in systems of lower mass since the balance between the gravitational forces and the energetic processes happening in the core of galaxies (mostly linked to massive black holes) changes in favour of the latter (Giodini et al. 2010). The signal to noise of weak lensing observations (in magenta) determining how well we can measure the total mass of the system, increases for systems of larger mass. These opposite behaviours define a 'sweet spot' in the mass range at 10^{14} M$_\odot$, where feedback is important and the mass of individual systems is measurable with weak lensing. With the CFHTLS, we can study systems exactly in this mass range (yellow shaded area).

and the weak lensing signal-to-noise ratio as a function of cluster mass. The ratio of the mechanical and binding energy is the average relationship from fig. 1 in Giodini et al. (2010), the weak lensing signal to noise is based on Hamana, Takada & Yoshida (2004).

We use lensing measurements of individual systems from the Canada–France–Hawaii Telescope Lensing Survey (CFHTLenS) and *XMM–Newton* X-ray observations from the *XMM*-CFHTLS survey. We refer to this sample as CFHTLS in this paper. This sample also includes one system from the *XMM*-LSS survey. We also include lower mass systems from COSMOS (Kettula et al. 2013b) and massive clusters from CCCP (Hoekstra et al. 2012; Mahdavi et al. 2013; Hoekstra et al. 2015) in order to study the mass dependence of the scaling relations. Combining the data from these three surveys allows us to constrain weak lensing calibrated scaling relations using a long mass baseline spanning approximately two orders of magnitude.

As pedagogically illustrated in appendix A of Mantz et al. (2010) scaling relations are affected by both Malmquist and Eddington bias. Both Malmquist and Eddington bias will only affect the relations in case of covariance between the intrinsic scatters of the observable used for cluster detection and the measurables under investigation. The effect of Eddington bias cannot be eliminated in the presence of intrinsic scatter about the mean relation (Eddington 1913) – because of the interplay between the steep decline at high masses of the mass function and intrinsic scatter of luminosity and temperature, it is more likely that lower mass systems scatter towards a higher luminosity or temperature, than vice versa. This renders massive clusters hotter and more luminous for their mass than intermediate-mass systems, whereas this is less of an issue for the low and intermediate-mass samples, where the mass function is flatter. In order to understand the mass dependence of the scaling relations, the effect of observational biases have to be considered. As shown by e.g. Rykoff et al. (2008) and Mantz et al. (2015), these effects can be modelled.

Clusters typically undergo several mergers during their formation, leading to a varying degree of substructure and triaxial asymmetry. As our sample contains only measurements of individual systems, we are able to study the effects of the merger and residual activity on the scaling relations by dividing our sample into subsamples of relaxed and non-relaxed systems by the amount of substructure.

Finally, galaxy cluster measurements are affected by cross-calibration uncertainties of X-ray detectors. This has been shown by the International Astronomical Consortium for High Energy Calibration IACHEC[1] (Nevalainen, David & Guainazzi 2010; Kettula, Nevalainen & Miller 2013a; Schellenberger et al. 2015), and independently by e.g. Snowden et al. (2008), Mahdavi et al. (2013), Donahue et al. (2014) and Israel et al. (2015). These studies indicate that cluster temperatures measured with the *Chandra* observatory are typically ∼10–15 per cent higher than those measured with *XMM*, whereas luminosities tend to agree to a few per cent. By investigating stacked residuals, the reported discrepancies can be accounted for by differences in the energy dependence of the effective area (Kettula, Nevalainen & Miller 2013a; Read, Guainazzi & Sembay 2014; Schellenberger et al. 2015).

The lensing measurements are presented in Section 2.1 and X-ray observations in Section 2.2. We derive the lensing masses in Section 3 and present the scaling relations between lensing mass and X-ray luminosity and temperature in Section 4. We include bias corrections, and study the effects of cluster morphology and X-ray cross-calibration. Finally, we discuss our results in Section 5, and summarize our work and present our conclusions in Section 6. We denote scaling relations as *Y–X*, with *Y* as the dependent variable (*y*-direction) and *X* as the independent variable (*x*-direction). We assume a flat Λ cold dark matter cosmology with $H_0 = 72$ km s^{-1} Mpc^{-1}, $\Omega_M = 0.30$ and $\Omega_\Lambda = 0.70$. All uncertainties are at 68 per cent significance, unless stated otherwise.

2 DATA

2.1 The CFHTLenS

The CFHTLenS is based on the Canada–France–Hawaii Telescope Legacy Survey (CFHTLS), where a total area of 154 deg^2 was imaged in five optical bands ($u*g'r'i'z'$). The data are spread over four distinct contiguous fields. The northern field W3 (∼44.2 deg^2) lacks X-ray coverage, but large fractions of the three equatorial fields (W1: ∼64 deg^2;W2: ∼23 deg^2;W4: ∼23 deg^2) were observed by *XMM–Newton* as part of the *XMM*-CFHTLS survey (Section 2.2).

The deep, multicolour data enable the determination of photometric redshifts of the sources (Hildebrandt et al. 2012) which are used to improve the precision of the lensing mass estimates by taking advantage of the redshift dependence. The *i'*-band data, which reach $i_{AB} = 25.5$ (5σ), are used for the lensing measurements because of the excellent image quality. To determine an accurate lensing signal from these data also requires a special purpose reduction and analysis pipeline which was developed and tested by us and is described in detail in Heymans et al. (2012) and Erben et al. (2013). We discuss some of the key steps in the weak lensing analysis, but refer the interested reader to the aforementioned CFHTLenS papers for a more detailed discussion.

A critical step in the weak lensing analysis is the accurate measurement of galaxy shapes. As the CFHT data consist of multiple *i'*-band exposures (typically seven), the algorithm needs to be able

to account for the varying point spread function (PSF) between exposures. The Bayesian fitting code LENSFIT (Miller et al. 2007, 2013) was used for this purpose. The resulting catalogue[2] includes measurements of galaxy ellipticities, ϵ_1 and ϵ_2, which can be used as estimators of the shear with an inverse variance weight w. Image simulations were used to determine additional empirical shear calibration corrections, which depend on signal to noise and galaxy size. These are described in Miller et al. (2013) and Heymans et al. (2012). These papers also present a number of tests to identify residual systematics. A key test is the measurement of the correlation between the PSF orientation and the corrected galaxy shape. Heymans et al. (2012) found that 75 per cent of the data pass this test and thus can be used in the cosmological analyses (Benjamin et al. 2013; Heymans et al. 2013; Kilbinger et al. 2013; Simpson et al. 2013; Kitching et al. 2014).

Cosmic shear studies are very sensitive to such residual correlations. In this paper, however, we measure the ensemble azimuthally averaged signal around a large number of low-mass clusters. As is the case for the study of the lensing signal around galaxies (Velander et al. 2014; Hudson et al. 2015), this measurement is much more robust against residual (additive) biases. Therefore we follow Velander et al. (2014) and use all CFHTLenS fields in our analysis. Six of our clusters reside within 5 arcmin of the image edges. As the PSF varies across the field of view, it is different from the central and outer regions of a pointing. As an additional sanity check of the reliability of our cluster masses, we therefore compare the masses of these six clusters to the other ones. We do not find any systematic difference with respect to the scaling relations.

Hildebrandt et al. (2012) present measurements of the photometric redshifts for the sources using the Bayesian photometric redshift code BPZ (Benítez 2000). Importantly, the PSF was homogenized between the five optical bands, which improves the accuracy of the photometric redshifts across the survey. The robustness of the photometric redshifts was tested in Hildebrandt et al. (2012) and Benjamin et al. (2013).

To ensure that robust shape measurements and reliable redshift estimates are available, we limit the source sample to those with $0.2 < z_{BPZ} < 1.3$ and $i' < 24.7$. The selection yields a scatter in photometric redshift in the range $0.03 < \sigma < 0.06$ with outlier rates smaller than 10 per cent (Hildebrandt et al. 2012). We also exclude galaxies that have the flag MASK > 0 as their photometry and shape measurement may be affected by image artefacts. The resulting sample has a weighted mean source redshift of $\langle z \rangle = 0.75$ and an effective number density of $n_{eff} = 11$ arcmin^{-2}.

2.2 The *XMM*-CFHTLS survey

11 clusters with X-ray flux significance greater than 20, corresponding to a minimum of 400 photons sufficient for reliable temperature measurements, have been observed by *XMM–Newton* as a part of the *XMM*-CFHTLS survey (PI: Finoguenov, see Mirkazemi et al. 2015). We also include one cluster (XID102760) from the CFHTLS W1 field which has been observed as a part of the *XMM*-LSS survey, with the analysis presented in Gozaliasl et al. (2014). The clusters have been identified from *ROSAT* All Sky Survey data, through optical filtering using CFHTLS multiband data and spectroscopic follow-up with HECTOSPEC/MMT Mirkazemi et al. (2015).

When compared to existing samples of galaxy clusters and groups, *XMM*-CFHTLS covers an interesting range of properties,

---

[1] http://web.mit.edu/iachec/

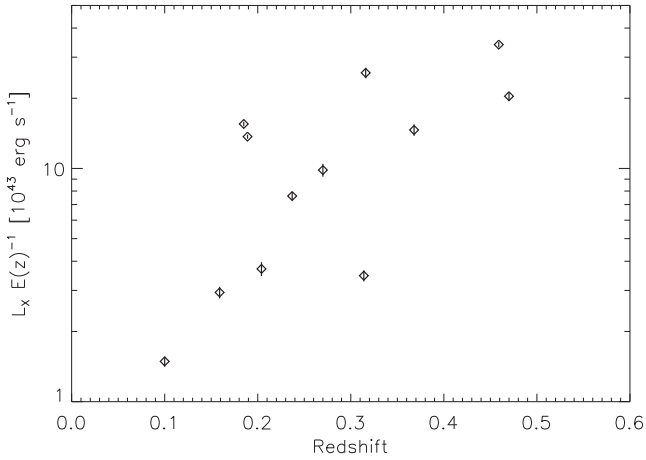[2] http://cfhtlens.org/astronomers/data-store

Figure 2. X-ray luminosity versus redshift for our cluster sample selected from *XMM*-CFHTLS (Mirkazemi et al. 2015).

bridging the intermediate mass range between groups and clusters. Because of the combination of a wide area with a moderately deep X-ray coverage, *XMM*-CFHTLS contains more low-mass systems at intermediate redshift than other *XMM* cluster samples such as REXCESS (Böhringer et al. 2007) or LocuSS (Smith et al. 2005), but not as low mass as those in COSMOS (Scoville et al. 2007). The typical system in *XMM*-CFHTLS is a low-mass cluster with a mean total mass of $\sim 10^{14}$ M$_\odot$, so that we can call these Virgo-sized systems (Fig. 2).

In order to efficiently find the clusters in the full area of the CFHTLS survey, we used ROSAT All Sky Survey (RASS, Voges et al. 1999) sources and identify them using CHFTLS photometric data and studied their masses using the combination of shape measurements and photometry. This X-ray selection of clusters for the scaling relation studies introduces a bias to the resulting scaling relation. The straightforward application is in using exactly the same quantity that has been used in the selection, which is a total X-ray luminosity L. Although we do not include the scaling relation with total L in this study, it is important to mention that the calculation of bias needs to be modified to account for the Eddington bias associated with the detection of sources in RASS data. The flux limit of the RASS data is formally 10^{-13} erg s^{-1} cm^{-2} in a 0.5–2 keV energy band, corresponding to 4 counts. A number of systems with a mean expected number of counts below the RASS limit of 4 that have been upscattered to over 4 are expected to be selected as well. For the scaling relations this leads to a *reduction* of bias. Following the formulation of Vikhlinin et al. (2009), we can write the bias correction as

$$b(\ln L_o) = \frac{\int_{-\infty}^{+\infty} (\ln L - \ln L_0) P(T|C(\ln L, z)) e^{\frac{(\ln L - \ln L_o)^2}{2\sigma^2}} \, d\ln L}{\int_{-\infty}^{+\infty} P(T|C(\ln L, z)) e^{\frac{(\ln L - \ln L_o)^2}{2\sigma^2}} \, d\ln L},$$

(1)

where T is the RASS count threshold, $C(x, z)$ are the predicted RASS counts from a cluster at a redshift z with luminosity L, $P(T|C(\ln L, z))$ is the probability of detection, σ is the scatter of the scaling relation. The bias for the average flux of the sources at the detection limit is 1.5 counts, leading to an average limit of 7×10^{-14} erg s^{-1} cm^{-2}, which is lower than the nominal RASS flux limit. *XMM–Newton* follow up removes this uncertainty from the flux and confirms the effect. For bias calculation due to the flux limit for a putative survey with high statistics, the Poisson term should be replaced by a

Gaussian around the flux limit. Most known clusters (e.g. REFLEX, NORAS, MACS), however, are selected from RASS down to count limits where Poisson effects are important. In this case equation (1) should be used.

The selection effects on the scaling relations involving other parameters than total luminosity depend on the covariance with the scatter. Since we work with core-excised temperature T_X and luminosity L_X, both measured inside 0.1–1 R_{500},[3] the bias due to selection on full luminosity L can only be present if there is a covariance in the scatter between the full luminosity and core-excised T_X and L_X. For example if cool core clusters have slightly different properties in the outskirts, some residual bias might be present (Zhang et al. 2011). However, at present the evidence for this effect is very marginal and we have decided not to correct for it. By determining the scaling relations separately for relaxed and unrelaxed clusters, we remove the effects of such residual biases.

For calculating L_X, we used the full aperture (0.1–1 R_{500}) and the measured temperature for K-correction, reducing the scatter associated with the assumption of the shape of the emission and predicting temperatures using the L_X–T_X relation. As X-ray selection preferentially detects relaxed clusters (due to cool cores) and the gas distribution generally displays stronger spherical symmetry than the underlying dark matter distribution, we did not consider orientation dependence in cluster selection. As we expect the contribution from triaxiality to be minimal, we assume spherical symmetry. We study the validity of this assumption is Section 5.4.

In measuring the temperature, we only use data from the EPIC-pn instrument, and performed a local adjustment of the background in addition to the use of stored instrument background, as in Finoguenov, Böhringer & Zhang (2005) and Pratt et al. (2007), since the clusters occupy only a small part of the detector. In the spectral analysis, we used the 0.5–7.5 keV energy band, excluding the 1.4–1.6 keV interval affected by instrumental line emission. We used SAS version 13.5.0 and corresponding calibration files to construct the responses.

3 WEAK LENSING SIGNAL

The differential deflection of light rays by an intervening lens leads to a shearing (and magnification) of the images of the sources (see e.g. Hoekstra et al. 2013, for a recent review on gravitational lensing studies of clusters). The resulting change in ellipticity, however, is typically much smaller than the intrinsic source ellipticity and an estimate for the shear is obtained by averaging the shapes of an ensemble of source galaxies.

As the survey volume increases, the massive systems are found at higher redshift. Unfortunately, the lensing signal decreases as the lens approaches the source redshift. This is because the amplitude of the lensing signal is inversely proportional to the critical surface density Σ_{crit} given by

$$\Sigma_{crit} = \frac{c^2}{4\pi G} \frac{D_s}{D_l D_{ls}},$$

(2)

where D_l is the angular diameter distance to the lens, D_s the angular diameter distance to the source, and D_{ls} the angular diameter distance between the lens and the source.

Hence the redshift dependence of the lensing signal and the noise due to the intrinsic shapes of the finite number of sources, limit both

[3] The spherical overdensity radius inside which the density is 500 times the critical density.

the mass and redshift range for which individual cluster masses can be measured. To ensure a sufficient number density of background galaxies, we limit the analysis to clusters with $z < 0.6$.

To determine the mass, it is convenient to azimuthally average the tangential shear $\langle \gamma_T \rangle$ as a function of radius from the lens, and fit a parametrized model to the signal. The LENSFIT measurements yield ellipticities ϵ_1 and ϵ_2, and the tangential shear is the projection perpendicular to the direction (with azimuthal angle ϕ) connecting the source galaxy and the lens. It is given by

$$\gamma_T = -(\epsilon_1 \cos(2\phi) + \epsilon_2 \times \sin(2\phi)). \tag{3}$$

It is also convenient to measure the cross-shear

$$\gamma_X = -(\epsilon_1 \sin(2\phi) - \epsilon_2 \times \cos(2\phi)), \tag{4}$$

whose azimuthal average is expected to vanish in the absence of systematic effects and is therefore used as a diagnostic. Note that we assume that the images are oriented randomly in the absence of lensing. Although this assumption may not hold in general (see e.g. Heymans et al. 2013), the amplitude is found to be small, but also it should not contribute to the tangential shear around lenses.

As discussed in Section 2.1 we only use sources with $i' < 24.7$, to ensure a robust shape measurement and we limit our sample to $0.2 < z < 1.3$, to ensure the robustness of the photometric redshifts (Hildebrandt et al. 2012). To minimize the contamination of cluster members in our source sample, we consider only source galaxies with a photometric redshift larger than $z_{\text{lens}}+0.15$. The redshift cut of 0.15 is a conservative one, and results in negligible contamination of cluster galaxies in the source sample. Including sources even closer to the lens redshift would not lead to a large improvement in signal to noise, as their lensing efficiencies are small. As the redshifts of our clusters are <0.6, the photo-z errors of the sources are almost flat close to the lens redshift (Hildebrandt et al. 2012), and the photo-z cut needs not be redshift dependent.

Thus, we sort the source galaxies in 15 equally sized radial bins from 0.15 Mpc from the centre of the lens (in our case the low-mass cluster) out to a radius of 3 Mpc. We define the centre as the location of the X-ray peak. In each bin, we perform a weighted average of the lensing signal as

$$\langle \Delta\Sigma \rangle (r) = \frac{\sum w_i \Sigma_{\text{crit},i} \gamma_{\text{T},i}(r)}{\sum w_i}, \tag{5}$$

where the lensing weight w_i quantifies the quality of the shape measurement (see Miller et al. 2013, for details). We compute $\Sigma_{\text{crit},i}$ by integrating over the redshift distribution of each source galaxy. Secondly, we apply a weight of $\Sigma_{\text{crit}}^{-2}$ to each lens-source pair, effectively down-weighing source galaxies that are close in redshift to the lens. As mentioned in Section 2.1 the LENSFIT output ellipticities need to be corrected for a multiplicative bias that depends on signal to noise and size $m(\nu_{\text{SN}}, r_{\text{gal}})$. As discussed in Miller et al. (2013), simply dividing the shear for each galaxy by a factor $(1 + m)$ would lead to a biased estimate of the average. Instead, we compute the corrected shear as follows:

$$\langle \Delta\Sigma^{\text{cor}} \rangle (r) = \frac{\langle \Delta\Sigma \rangle (r)}{1 + K(r)}, \tag{6}$$

where the correction is given by

$$1 + K(r) = \frac{\sum w_i [1 + m(\nu_{\text{SN}}, r_{\text{gal}})]}{\sum w_i}, \tag{7}$$

with ν_{SN} stands for the signal-to-noise ratio of the galaxy and r_{gal} the size. The error on the shear signal is computed by taking the inverse square root of the sum of the weights, and accounts for intrinsic shape noise as well as measurement noise.

To estimate cluster masses, we assume that the matter density is described by an NFW profile (Navarro, Frenk & White 1997), which is found to be a good approximation to simulated profiles in *N*-body simulations of collisionless cold dark matter. The density profile is given by

$$\rho(r) = \frac{\delta_c \rho_{\text{crit}}}{\frac{r}{r_s} \left(1 + \frac{r}{r_s} \right)^2}, \tag{8}$$

where $\rho_{\text{crit}} = 3H^2(z)/8\pi G$ is the critical density of the Universe at the lens redshift z and $H(z)$ is the corresponding Hubble parameter. The scale radius r_s is related to the virial radius r_{vir} by the concentration parameter $c_{\text{vir}} = r_{\text{vir}}/r_s$ and δ_c is related to c_{vir} by

$$\delta_c = \frac{\Delta_{\text{vir}}}{3} \frac{c_{\text{vir}}^3}{\ln(1 + c_{\text{vir}}) - \frac{c_{\text{vir}}}{1 + c_{\text{vir}}}}, \tag{9}$$

where Δ_{vir} is the average overdensity inside r_{vir}. Alternatively, we can express the mass in terms of M_Δ, the mass contained within a radius r_Δ where the mean mass density is $\Delta \times \rho_{\text{crit}}$. Results are commonly listed for $\Delta = 200$ and 500.

Numerical simulations also indicate that the virial mass M_{vir} and the concentration are correlated, with more massive systems having lower values for c_{vir}. Here, we use the results from Duffy et al. (2008), which give

$$c = 5.71 \times \left(\frac{M_{200}}{2 \times 10^{12} h^{-1}} \right)^{-0.084} \times (1 + z)^{-0.47}. \tag{10}$$

Analytic expressions for the tangential shear of NFW profiles have been derived by Wright & Brainerd (2000) and Bartelmann (1996). We fit the NFW model shear to the profiles shown in Fig. 3 and indicate the best-fitting model by the solid line. The coloured region indicates the 68 per cent region for the model. As we measure M_{200} from the NFW profile using the mass–concentration relation in equation (10), we have one free parameter for 15 radial bins giving 14 degrees of freedom (we note that cluster XID210640 falls in the middle of a large stellar halo mask and lacks data on smaller scales). We test the best-fitting NFW profile against the null hypothesis that the tangential shear signal is zero and show the reduced χ^2 values in Fig. 3. We use the best-fitting NFW profile to rescale virial mass to M_{500}. The resulting values for M_{200} and M_{500} are listed in Table 1.

These are indeed the most massive clusters in the *XMM*-CFHTLS data, but the observed lensing signal is nevertheless quite sensitive to contributions from uncorrelated large-scale structure along the line of sight (Hoekstra 2001; Hoekstra et al. 2011) or substructure and triaxial shape of the cluster halo (Corless & King 2007; Meneghetti et al. 2010; Becker & Kravtsov 2011). Such structures modify the observed tangential shear profile. Both effects are an additional source of noise, whereas the latter might lead to biased mass estimate if we fit an NFW model to the data.

The χ^2 values of the NFW profile fits shown in Fig. 3 show that the data are well described by a single NFW profile. However, we note that for XID210910 a secondary group is detected in the X-ray image, which would tend to bias the NFW mass high.

3.1 Systematics in mass estimates

The accuracy of the scaling relations depends on the ability to measure unbiased cluster masses. In this section, we investigate different systematic effects that can bias our lensing masses.

As we fit the density profiles down to a radial range of 150 kpc, the resulting masses can be affected by the mass–concentration relation assumed for the NFW profile. This was explored by Hoekstra et al.
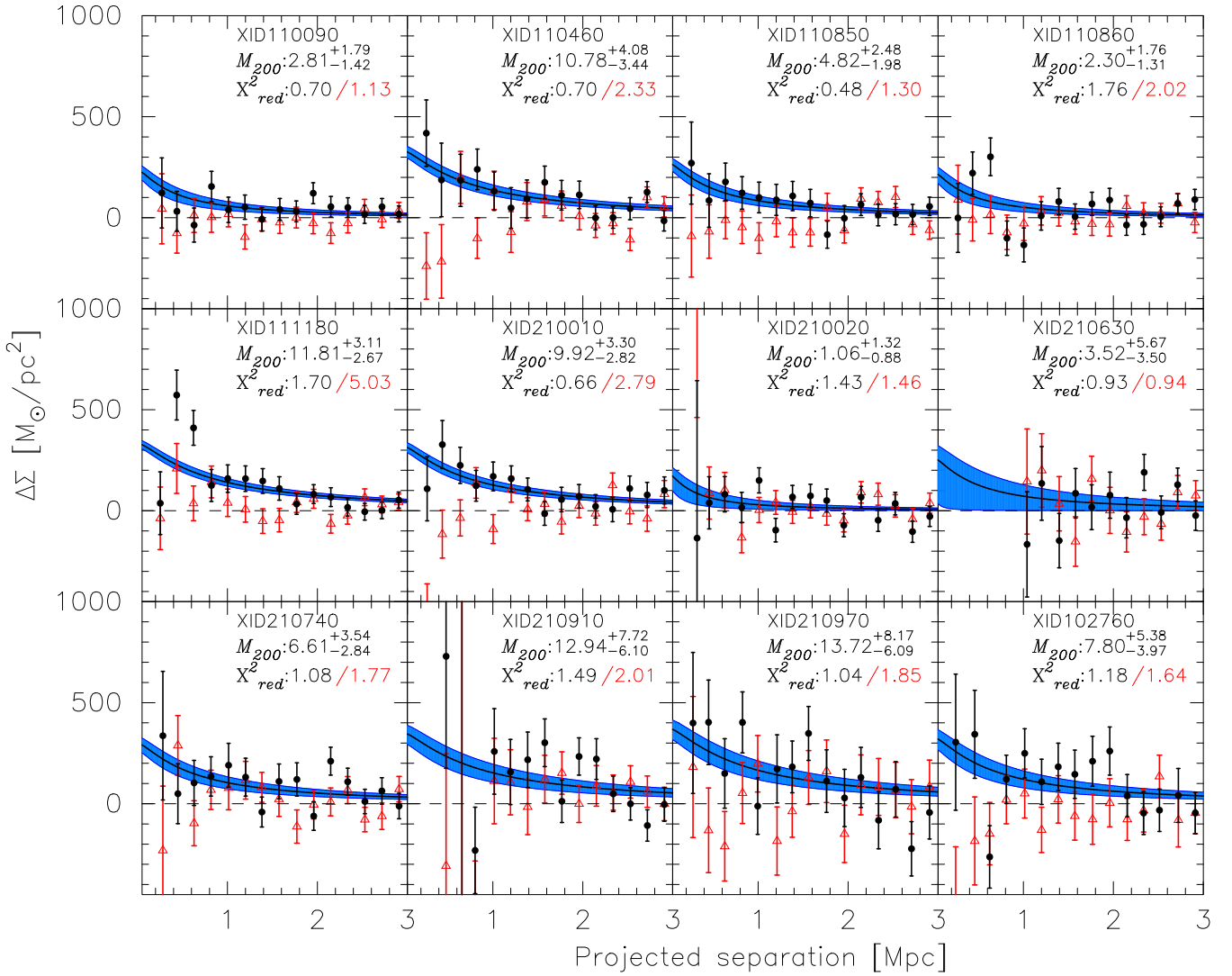
Figure 3. Shear profiles out to 3 Mpc for the individual X-ray clusters measured using CFHTLenS data that were detected with an X-ray flux significance higher than 20, corresponding to a minimum of 400 photons. The blue shaded line shows the uncertainty on the best-fitting profile. Each panel shows the mass M_{200} and the error of the mass in units of 10^{14} M$_\odot$, measured shear profiles and the χ^2 values for the NFW profile fit to the tangential shear (black circles). The cross-shear and the χ^2 value of the null hypothesis that the tangential shear signal is zero are shown in red. Cluster XID210640 falls in the middle of a large stellar halo mask and lacks data on smaller scales.

(2012), who showed that the sensitivity to the mass–concentration depends on the fit range and overdensity Δ. They found their masses using a fit range of 0.5–2.0 Mpc to be most stable with $\Delta = 1000$. To investigate how sensitive our masses are to the selected mass–concentration relation, we fit the NFW profiles assuming the relation of Dutton & Macciò (2014). We find that the average ratio of best-fitting masses using Dutton & Macciò (2014) to Duffy et al. (2008) is 0.92 ± 0.04, i.e. Dutton & Macciò (2014) results on average in lower masses by 2σ (see Fig. 4). As an additional test, we also measured our masses by excluding the central 0.5 Mpc and find perfect agreement with our reported mass estimates. The average ratio of best-fitting masses is 0.99 ± 0.11 (see Fig. 4).

Simulations by Becker & Kravtsov (2011) suggest that extending the fit range beyond the virial radius may bias lensing masses low by 5–10 per cent due to the correlated large-scale structure. To test this, we adopt an upper fit range of 2 Mpc. In this case, we find that the average ratio of the best-fitting masses is 1.15 ± 0.49. If fitting beyond the virial radius would bias our mass estimates low,

the ratio of the best-fitting masses should be larger for low-mass systems with smaller virial radii than for massive clusters. We are not able to detect this trend in the data (see Fig. 4).

In the lensing measurement, we compute the mean lensing efficiency $\langle D_{ls}/D_s \rangle$ for each source by integrating over the full stacked photo-z posterior probability distribution $P(z)$. Since the relation between lensing efficiency and redshift is non-linear, this could introduce a bias if the stacked $P(z)$ is not a fair representation of the actual redshift distribution of the sources. To estimate its size, we consider a single lens–source pair. For the lens, we adopt a redshift of 0.2. For the source, we assume a redshift probability distribution that is representative for objects in CFHTLenS (see Hildebrandt et al. 2012), i.e. we describe the stacked $P(z)$ by a Gaussian with a mean of 0.7 and a standard deviation of 0.05, plus a second Gaussian with a standard deviation of 0.5 (but with the same mean) that contains 7 per cent of the total probability, to account for an outlier fraction of 7 per cent. We compare the input D_{ls}/D_s to the one that is averaged over the stacked $P(z)$, and find that the latter is biased

Table 1. Table of X-ray measurements and weak lensing masses for systems in our sample.

XID	RA (deg)	DEC (deg)	z	L_X (10^{43} erg s^{-1})	T_X (keV)	M_{200} (10^{14} M$_\odot$)	M_{500} (10^{14} M$_\odot$)	D_{BCG} (kpc)
110090	36.2713	−9.8381	0.159	3.16 ± 0.18	3.62 ± 0.79	$2.81^{+1.79}_{-1.42}$	$2.00^{+1.28}_{-1.02}$	17
110460	35.998	−8.5956	0.27	11.19 ± 0.71	7.25 ± 3.19	$10.78^{+4.08}_{-3.44}$	$7.45^{+2.82}_{-2.38}$	28
110850	33.6064	−6.4605	0.237	8.52 ± 0.35	2.39 ± 0.7	$4.82^{+2.48}_{-1.98}$	$3.38^{+1.74}_{-1.39}$	17
110860	36.3021	−6.3837	0.204	4.0 ± 0.28	3.87 ± 1.19	$2.30^{+1.76}_{-1.31}$	$1.64^{+1.26}_{-0.93}$	13
111180	37.9269	−4.8814	0.185	16.90 ± 0.37	5.0 ± 0.61	$11.81^{+3.11}_{-2.67}$	$8.23^{+2.17}_{-1.86}$	62
210010	133.0656	−5.5651	0.189	14.94 ± 0.29	4.88 ± 0.62	$9.92^{+3.30}_{-2.82}$	$6.93^{+2.31}_{-1.97}$	24
210020	134.6609	−5.4211	0.1	1.56 ± 0.08	1.65 ± 0.3	$1.06^{+1.32}_{-0.88}$	$0.77^{+0.96}_{-0.64}$	431
210630	133.5554	−2.3499	0.368	17.53 ± 0.98	5.31 ± 2.48	$3.52^{+5.67}_{-3.50}$	$2.45^{+3.95}_{-2.44}$	29
210740	135.4147	−1.9799	0.314	4.04 ± 0.22	4.59 ± 1.57	$6.61^{+3.54}_{-2.84}$	$4.58^{+2.45}_{-1.97}$	21
210910	135.3770	−1.6532	0.316	29.95 ± 1.56	5.04 ± 2.42	$12.94^{+7.72}_{-6.10}$	$8.87^{+5.29}_{-4.18}$	30
210970	133.0675	−1.0260	0.459	42.81 ± 1.07	5.35 ± 1.18	$13.72^{+8.17}_{-6.09}$	$9.25^{+5.50}_{-4.10}$	42
102760	35.4391	−3.7712	0.47	25.88 ± 1.13	8.2 ± 5.55	$7.80^{+5.38}_{-3.97}$	$5.30^{+3.66}_{-2.70}$	32

Notes. XID is the X-ray identification number in the *XMM*-CFHTLS survey, RA and DEC are the coordinates of the cluster centre defined by the X-ray peak, z the redshift of the cluster, T_X and L_X the X-ray temperature and luminosity, M_{200} and M_{500} the spherical overdensity masses with respect to the critical density and D_{BCG} the offset between the BCG and X-ray peak.
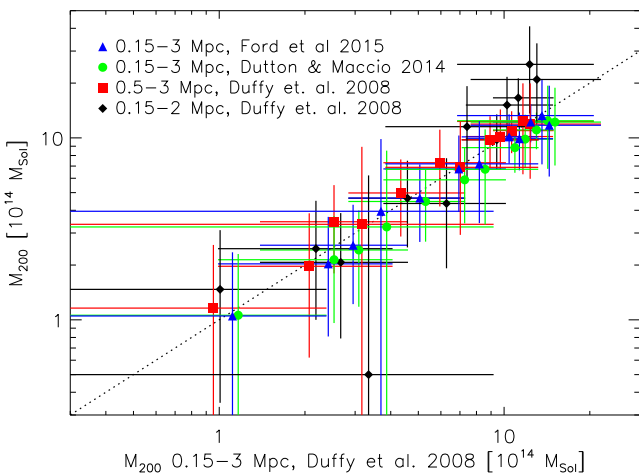

Figure 4. Comparison of mass measurements assuming different mass–concentration relations, radial fit ranges or background galaxy filtering to the mass measurements adopted in this work.

low by 1 per cent. Repeating the test for a lens at a redshift of 0.5 and a mean source redshift of 0.9, we find a similar bias.

If not properly accounted for, dilution by foreground galaxies can bias the mass measurements. Using the $P(z)$ modelling above, we compute a mass dilution by foreground galaxies of 3.5 per cent. As a final test, we re-measure the masses using the same selection criteria for background galaxies as Ford et al. (2015), i.e. that the peak of the galaxy's $P(z)$ is higher than the redshift of the cluster and that at least 90 per cent of the galaxy's $P(z)$ is at a higher redshift than the cluster. In this case, we find that the best-fitting masses are consistent with our measurements, with an average ratio of 0.97 ± 0.08 (see Fig. 4). We also note that in case our mass measurements would be significantly diluted by foreground galaxies, the expected ratio would be higher than unity.

4 SCALING RELATIONS

The combination of X-ray and CFHTLenS weak lensing data is ideal for calibrating cluster mass proxies in the low-mass cluster regime. We present our fitting method, sample, bias corrections, and morphological classification of systems in Section 4.1. In Sections 4.2, 4.3 and 4.4, we present the scaling between weak lensing mass, core-excised X-ray luminosity and temperature, and discuss the global scaling properties (we explore the mass and morphology dependence of the relations in Sections 5.3 and 5.4). Finally, we study the effects of X-ray cross-calibration in 4.5.

4.1 Fitting method

The self-similar prediction for the scaling relation between two quantities A and B, such as mass and luminosity or luminosity and temperature, is a power-law, where the predicted value of slope α varies for the different relations (Kaiser 1986). Here, we assume such a power-law form given by

$$\log_{10} \frac{A \times E(z)^{n_A}}{A_0} = \log_{10}(N) + \alpha \times \log_{10} \frac{B \times E(z)^{n_B}}{B_0} \quad (11)$$

with A_0 and B_0 defining the pivot-point. $E(z)$ gives the scaling of overdensity with redshift and it is defined as

$$E(z) = \frac{H(z)}{H_0} = \sqrt{\Omega_M (1 + z)^3 + \Omega_\Lambda}. \quad (12)$$

n_A and n_B give the $E(z)$ dependence of quantities A and B. For mass n_A or n_B is 1, for L_X it is −1 and for T_X 0.

We let both the slope α, normalization $\log_{10}(N)$ and intrinsic scatter $\sigma_{\log(A|B)}$ vary freely in the fits. We use the Bayesian linear regression routine of Kelly (2007) with the Metropolis–Hastings sampler to find the best-fitting parameters. The routine includes intrinsic scatter in the dependent variable (i.e. *y*-direction) $\sigma_{\log(A|B)}$, which we expect to follow a lognormal distribution. We define best-fitting parameters as the median of the single parameter posterior distributions and errors as the values corresponding to the 68th percentiles.

In order to improve the precision and to study the mass dependence of the relation, we include measurements of 10 individual

low-mass systems from the Cosmic Evolution Survey (COSMOS) and 48 individual high-mass systems from the Canadian Cluster Comparison Project (CCCP). We utilize the three surveys making up our sample as overlapping mass bins, with COSMOS forming the low-mass, CFHTLS intermediate-mass and CCCP the high-mass bin, and fit the scaling relations independently for each of the surveys.

COSMOS data, lensing and temperature measurements are presented in Kettula et al. (2013b). The COSMOS systems have lensing masses based on deep *HST* imaging and 30+ band photometric redshifts, and X-ray measurements obtained with *XMM–Newton*. We derive luminosities from the COSMOS data using the method presented in Section 2.2 in this work (see Table A1). For the CCCP sample, we use recent lensing mass measurements presented in Hoekstra et al. (2015) measured assuming an NFW density profile and the Duffy et al. (2008) mass–concentration relation and X-ray measurements obtained with both *Chandra* and *XMM–Newton*. We derive core-excised L_X using the 0.1–2.4 keV band for the CCCP systems using the method described in Mahdavi et al. (2013, see also Mahdavi et al. 2014) and use the core-excised temperatures from Mahdavi et al. (2013).[4] The soft band L_X measurements are given in Table A2. *Chandra* observations of CCCP clusters are adjusted to match *XMM–Newton* calibration. This gives us a sample of 72 individual systems, with $T_X \sim 1$–12 keV, $L_X \sim 10^{43}$–10^{45} erg s^{-1} and a mass from $\sim 10^{13}$ to a few times 10^{15} M$_\odot$.

We note that there are differences in the calibration of the lensing signal for these additional data sets, compared to CFHTLS. Furthermore, the CCCP data lack photometric redshift information which may impact the correction for contamination by cluster members. These uncertainties impact the masses at the 5–10 per cent level for individual clusters. We estimated the effect of the lensing calibration uncertainties by examining how the slopes of M–T_X and M–L_X relations change when decreasing the mass of all COSMOS systems by 5 per cent while increasing CCCP masses by 5 per cent and vice versa. We find that the effect is small at 3 and 5 per cent for M–T_X and M–L_X and do not include this effect in the quoted statistical uncertainties.

4.1.1 Bias correction

The Kelly (2007) regression method attempts to correct for sampling effects in the independent variable (*x*-direction). Since we deal with X-ray selected samples of galaxy clusters, we are thus able to correct for possible residual Malmquist bias due to the covariance between the studied parameter and the parameter used to select the clusters by keeping L_X or T_X as the independent variable. However, the regression method determines the scatter only for the dependent variable, and assumes no intrinsic scatter for the independent variable. Consequently, we first have to determine the scatter in L_X and T_X at fixed mass and add these to the statistical errors.

Therefore we first measure the global inverted relation with mass as the independent variable to determine the scatter in L_X and T_X. We assume that the intrinsic scatter of mass measurement using weak lensing with respect to the true mass is 0.2 in natural logarithm units (Becker & Kravtsov 2011), and add this value to the mass errors for every fit having mass as the independent variable. As shown by Vikhlinin et al. (2009), the value of the scatter is independent of a possible bias in the slope.

The correction term due to Eddington bias is

$$\sigma^2 \ln(10) \frac{\mathrm{d}\alpha(\ln(M))}{\mathrm{d} \ln(M)}$$

(Leauthaud et al. 2010), where sigma is the total (statistical and intrinsic) scatter for the parameter in dex, ln(10) is a correction term for using scatter in units of dex and α is a slope of the mass function. We compute the mass-function related term using the parametrization of van den Bosch (2002) and the assumed cosmology. The correction term for mass, L_X and T_X are computed individually for each system in the sample, and we subtract these from the measured values.

For total scatter in L_X and T_X, we use the summed square of the statistical errors and measured intrinsic scatter. The value for the total scatter in weak lensing masses, which correspond to the a convolution of the data quality and the intrinsic scatter, is assumed to be 0.3 in natural logarithm units. This value is used both as the total scatter term for mass and to smooth the theoretical mass function to establishing the derivative of the distribution of clusters as a function of weak lensing mass. Using weak lensing mass as opposed to the true mass yields smaller slopes for the mass function.

We refer to the measurements corrected for Eddington bias and scaling relations fitted to the corrected measurements as bias corrected (BC). The bias correction is discussed in more detail in Leauthaud et al. (2010). Contrary to Leauthaud et al. (2010), who used the global slope of the mass function, we use a local one for each system. In both cases we implicitly assume a strong covariance between the selection and observable. While both methods lead to small global changes, using the local slope leads to sizeable corrections in particular for the CCCP sample, which contains a large number of massive clusters at relatively high redshifts. We show the bias corrections for individual systems in Fig. 5 and list them in Appendix B.

As the Kelly (2007) fitting routine corrects for Malmquist bias in the independent variable, our bias-corrected M–L_X and M–T_X relations are fully corrected for observational biases, whereas there might be some residual covariance affecting the L_X–M, T_X–M and L_X–T_X relations. However, we expect the effect for the global relation to be small. We also explored fits performed individually for each survey (accounting separately for Malmquist bias) and combining the posterior distributions, but found that the combined posterior not to be as constraining as the combined data set.

4.1.2 Morphological classification

The distance between the brightest cluster galaxy (BCG) and X-ray surface brightness peak (D_{BCG}) has been shown to be a good indicator of the relaxation state by e.g. Poole et al. (2007) and Mahdavi et al. (2013). Large values for D_{BGC} indicate significant substructure typical for unrelaxed clusters. We are able to identify BCG locations using the *XMM*-CFHTLS optical photometry of Mirkazemi et al. (2015). For the *XMM*-LSS cluster XID102760, we use photometry of Gozaliasl et al. (2014). The location of the X-ray peaks are determined from X-ray photometry presented in this work. For COSMOS and CCCP systems, we use D_{BCG} values presented in Kettula et al. (2013b) and Mahdavi et al. (2013), respectively.

We classify clusters with $D_{BGC} < 3$ per cent of R_{200} as relaxed and those with $D_{BGC} \geq 3$ per cent of R_{200} as non-relaxed (which we refer to as mergers or merging clusters). Here, R_{200} is the radius inside which the mean density of the cluster corresponds to 200 times the critical density at the redshift of the system. For our sample, 3 per cent of R_{200} corresponds to 13–75 kpc and gives 55 relaxed

---

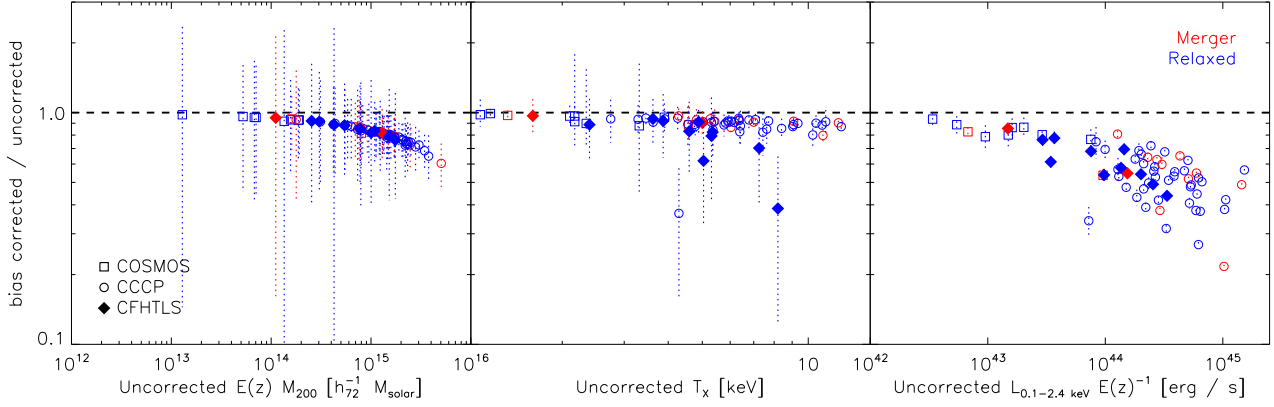[4] Available on http://sfstar.sfsu.edu/cccp/.

Figure 5. The values of the Eddington bias corrections applied to mass (left-hand panel), temperature (middle panel) and luminosity (right-hand panel). Blue and red dotted data show the residuals for individual merging and relaxed systems, squares indicate systems from COSMOS, circles from CCCP and solid diamonds from CFHTLS. Errors are the statistical errors of the measurements.
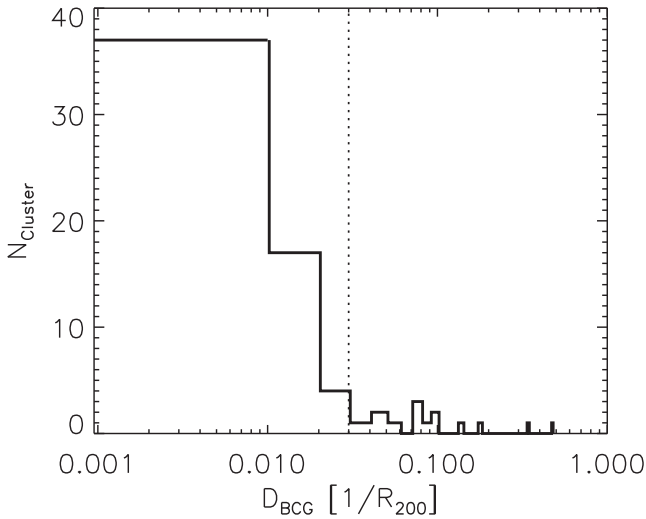

Figure 6. The distribution of offsets between X-ray peak and BCG D_{BGC}. D_{BGC} are given as fractions of R_{200}. The dotted vertical line separates between relaxed and merging clusters.

Figure 7. The scaling of core-excised X-ray temperature T_X to core-excised luminosity L_X. The black solid line and grey shaded region shows the best-fitting relation and statistical uncertainty fitted to all data, the red solid line shows the corresponding BC relation. The dotted line shows the relation fitted to relaxed clusters (blue data) and dashed line to merging clusters (red data). The dot–dashed and long dashed lines shows relations fitted independently to each survey and the red dashed line is the best-fitting uncorrected relation from Lovisari et al. (2015). Errors on data indicate statistical uncertainties.

systems and 15 non-relaxed merging systems (see Fig. 6). As the CFHTLS and COSMOS samples are selected on X-ray brightness and the CCCP sample, though originally selected on *ASCA* T_X, is consistent with well-defined flux-based samples (Mahdavi et al. 2013), we expect to find a large fraction of relaxed clusters with cool cores associated with high X-ray brightness peaks.

4.2 L_X–T_X relation

For the L_X–T_X relation, we adopt $L_0 = 10^{44}$ erg s^{-1} and $T_0 = 5$ keV. The resulting relations and fit parameters are shown in Figs 7–9, and Table 2.

The scatter in L_X at fixed temperature is $0.15^{+0.04}_{-0.04}$ for the uncorrected relation and $0.10^{+0.04}_{-0.04}$ for the BC relation. The slopes are steeper than the self-similar prediction of 2.0, we get $2.65^{+0.17}_{-0.17}$ in the uncorrected case and $2.52^{+0.17}_{-0.16}$ after bias correction.
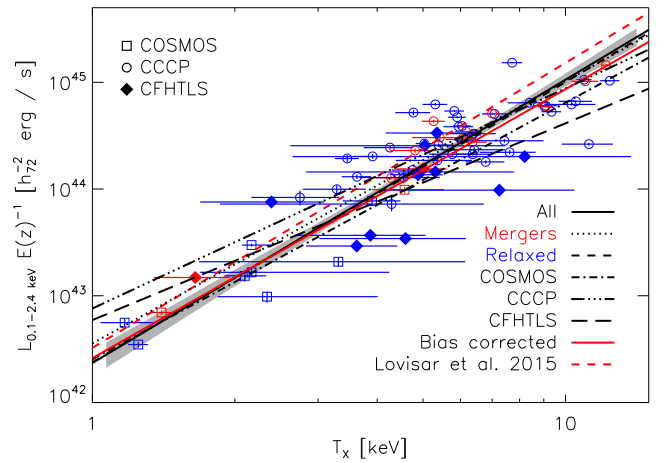
Lovisari et al. (2015) used *XMM–Newton* observations of a flux-limited set of nearby galaxy groups together with data of the HI-FLUGCS clusters from Hudson et al. (2010), resulting in a sample spanning a similar L_X and T_X range as ours. In Fig. 7, we compare their relation corrected for selection bias effects (using full luminosities and core-excised temperatures) to our core-excised relations. We find that their slope is consistent within the uncertainties with our relation, but they predict systematically higher luminosities at fixed temperature because they use total luminosities.

4.3 M–L_X relation

X-ray luminosity L_X is the observationally cheapest X-ray observable, requiring only source detection and redshift information for its measurement. Luminosity is hence the mass proxy choice for shallow X-ray surveys, making the mass–luminosity relation potentially a powerful cosmological instrument.
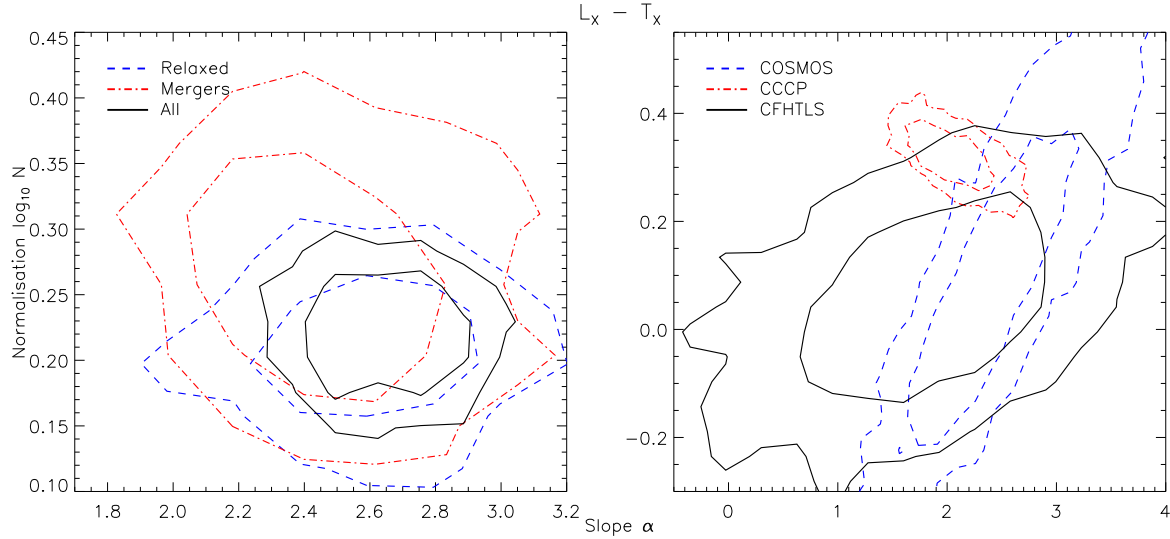
Figure 8. Confidence contours for the posterior distributions of slope and normalization at 68 and 95 per cent significance for the L_X–T_X relations fitted to each respective subsample.
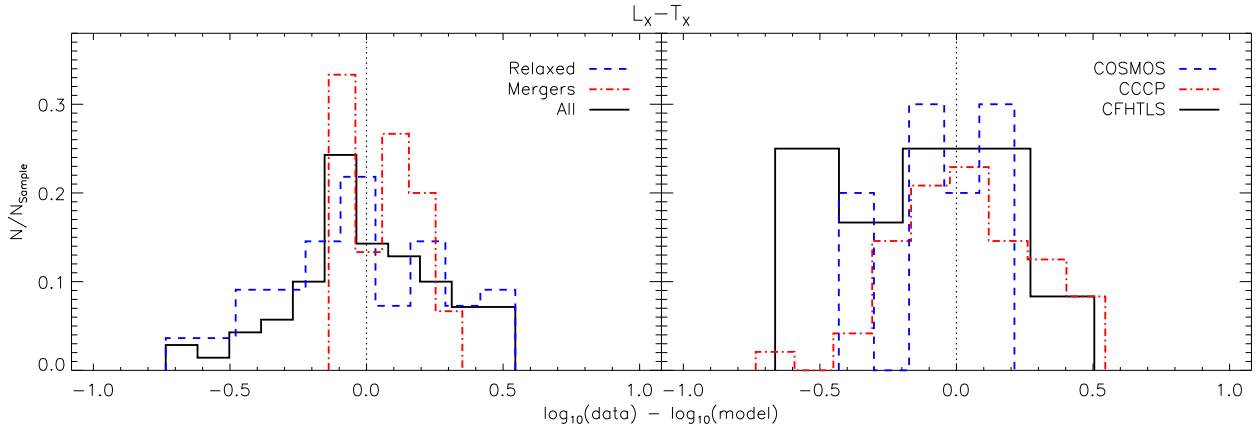

Figure 9. The distribution of residuals for each subsample with respect to the L_X–T_X relation fitted to the full sample. N_{Sample} is defined as the number of systems in each subsample.

As typically done in the literature, we opt to study the scaling of luminosity to the total mass of the halo given by M_{200}, (but also quote the parameters for scaling to M_{500}). For the M–L_X relations, we set L_0 to 10^{44} erg s^{-1} and M_0 to 3×10^{14} M$_\odot$. The resulting relations and fit parameters are shown in Figs 10–12 and Table 2.

The scatter in L_X at fixed mass is $0.33^{+0.03}_{-0.03}$ in the uncorrected case and $0.29^{+0.04}_{-0.03}$ in the BC case. We obtain a consistent slope for the BC and uncorrected relations, the uncorrected slope is $0.74^{+0.08}_{-0.08}$. The slope is consistent with the purely gravitational self-similar prediction of 0.75.

Currently the only other M–L_X relation spanning a similar mass range as ours using weak lensing mass calibration is that of Leauthaud et al. (2010). They derived non-core excised luminosities and lensing masses for stacked low-mass galaxy groups in the COSMOS field and combined them with higher mass systems from the literature. Their slope of 0.64 ± 0.03 is flatter than ours. The Leauthaud et al. (2010) relation predicts consistent luminosities with us at low masses, but leading to significant tension at high masses (see Fig. 10). In addition to the weak lensing measurements, the mass calibration of the low-mass Leauthaud et al. (2010) sample has been confirmed by magnification analysis (Ford et al. 2012; Schmidt et al. 2012) and clustering (Allevato et al. 2012).

4.4 M–T_X relation

The relation between mass and temperature is the most fundamental among the scaling relations because it provides the physical link between X-ray observations of galaxy clusters and the models of structure formation. If the only source of heating of the gas is gravitational and there is no efficient cooling, the gas temperature is a direct measure of the potential depth, and therefore of the total mass.

For the M–T_X relation, we opt to study the scaling to M_{500}, as is usually done in the literature (but we also quote the parameters of the relation for M_{200}). The best-fitting relations and fit parameters for $M_0 = 5 \times 10^{14}$ M$_\odot$ and $T_0 = 5.0$ keV are shown in Figs 13–15 and Table 2.

We find that T_X is a low-scatter mass proxy, the intrinsic scatter in temperature at fixed mass is $0.11^{+0.01}_{-0.01}$ in the uncorrected case and $0.06^{+0.02}_{-0.02}$ for the fully BC relation. The slope of the uncorrected relation is $1.68^{+0.17}_{-0.17}$. The bias correction results in a slightly shallower slope of $1.52^{+0.17}_{-0.16}$, which is fully consistent with the self-similar prediction of 1.50.

In Fig. 13, we also compare our relations to the best-fitting M–T_X relation from Kettula et al. (2013b), where we use CCCP with

Table 2. The fit parameters and intrinsic scatter with the corresponding statistical uncertainties of the scaling relations.

	α	$\log_{10}N$	$\sigma_{\log(A\mid B)}$
L_X–T_X			
All data	$2.65^{+0.17}_{-0.17}$	$0.23^{+0.03}_{-0.03}$	$0.15^{+0.04}_{-0.04}$
Bias corrected	$2.52^{+0.17}_{-0.16}$	$0.18^{+0.03}_{-0.03}$	$0.10^{+0.04}_{-0.04}$
Mergers	$2.46^{+0.27}_{-0.24}$	$0.27^{+0.06}_{-0.06}$	$0.10^{+0.07}_{-0.05}$
Relaxed	$2.62^{+0.22}_{-0.22}$	$0.21^{+0.04}_{-0.04}$	$0.20^{+0.05}_{-0.04}$
CFHTLS	$1.84^{+0.80}_{-0.76}$	$0.06^{+0.12}_{-0.13}$	$0.34^{+0.13}_{-0.09}$
COSMOS	$2.40^{+0.54}_{-0.46}$	$0.08^{+0.21}_{-0.19}$	$0.17^{+0.12}_{-0.09}$
CCCP	$2.06^{+0.29}_{-0.28}$	$0.32^{+0.04}_{-0.04}$	$0.13^{+0.04}_{-0.04}$
L_X–M_{200}			
All data	$1.13^{+0.10}_{-0.10}$	$-0.22^{+0.06}_{-0.06}$	$0.33^{+0.03}_{-0.03}$
Bias corrected	$1.27^{+0.16}_{-0.15}$	$-0.38^{+0.06}_{-0.06}$	$0.29^{+0.04}_{-0.03}$
M_{200}–L_X			
All data	$0.74^{+0.08}_{-0.08}$	$0.31^{+0.04}_{-0.04}$	$0.15^{+0.04}_{-0.04}$
Bias corrected	$0.74^{+0.09}_{-0.08}$	$0.40^{+0.03}_{-0.03}$	$0.10^{+0.04}_{-0.04}$
Mergers	$0.60^{+0.16}_{-0.15}$	$0.29^{+0.10}_{-0.11}$	$0.21^{+0.10}_{-0.09}$
Relaxed	$0.78^{+0.09}_{-0.09}$	$0.31^{+0.04}_{-0.05}$	$0.14^{+0.04}_{-0.04}$
CFHTLS	$0.66^{+0.35}_{-0.29}$	$0.47^{+0.09}_{-0.10}$	$0.15^{+0.12}_{-0.08}$
COSMOS	$0.83^{+0.46}_{-0.39}$	$0.35^{+0.37}_{-0.34}$	$0.28^{+0.21}_{-0.13}$
CCCP	$0.80^{+0.38}_{-0.29}$	$0.25^{+0.15}_{-0.21}$	$0.17^{+0.04}_{-0.05}$
M_{500}–L_X			
All data	$0.70^{+0.08}_{-0.07}$	$0.15^{+0.04}_{-0.04}$	$0.14^{+0.03}_{-0.03}$
T_X–M_{500}			
All data	$0.45^{+0.04}_{-0.04}$	$-0.02^{+0.02}_{-0.02}$	$0.11^{+0.01}_{-0.01}$
Bias corrected	$0.48^{+0.06}_{-0.06}$	$-0.03^{+0.02}_{-0.02}$	$0.06^{+0.02}_{-0.02}$
M_{500}–T_X			
All data	$1.68^{+0.17}_{-0.17}$	$0.08^{+0.03}_{-0.03}$	$0.14^{+0.03}_{-0.03}$
Bias corrected	$1.52^{+0.17}_{-0.16}$	$0.05^{+0.03}_{-0.03}$	$0.07^{+0.04}_{-0.04}$
Mergers	$1.43^{+0.32}_{-0.31}$	$0.05^{+0.07}_{-0.07}$	$0.18^{+0.09}_{-0.07}$
Relaxed	$1.78^{+0.22}_{-0.21}$	$0.09^{+0.03}_{-0.04}$	$0.15^{+0.04}_{-0.04}$
CFHTLS	$1.34^{+0.78}_{-0.73}$	$0.14^{+0.09}_{-0.10}$	$0.16^{+0.13}_{-0.08}$
COSMOS	$1.52^{+0.90}_{-0.82}$	$-0.14^{+0.34}_{-0.34}$	$0.29^{+0.21}_{-0.14}$
CCCP	$1.18^{+0.31}_{-0.29}$	$0.14^{+0.05}_{-0.05}$	$0.17^{+0.03}_{-0.03}$
M_{200}–T_X			
All data	$1.73^{+0.19}_{-0.17}$	$0.26^{+0.03}_{-0.03}$	$0.15^{+0.03}_{-0.03}$

Notes. α is the slope of the relation, $\log_{10}N$ the normalization and $\sigma_{\log(A\mid B)}$ the intrinsic scatter. BC relations are fitted to the full data set.

different temperature measurements as a high-mass sample and five clusters from the 160 Square Degree survey as an intermediate-mass sample to infer a scaling consistent the self-similarity. We find that the best-fitting relation of Kettula et al. (2013b) has a shallower slope than our uncorrected and BC relations, predicting somewhat lower temperatures for a given mass in the high-mass end.

4.5 X-ray cross-calibration

We investigated the effects of cross-calibration on scaling relations by modifying our *XMM*-based temperatures and luminosities to match *Chandra* calibration, allowing direct comparison to relations
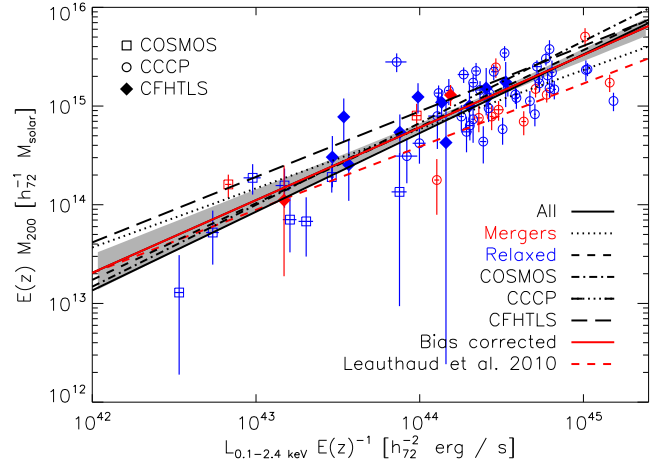

Figure 10. The scaling of mass M_{200} to core-excised luminosity L_X. The black solid line and grey shaded region shows the best-fitting relation and statistical uncertainty fitted to all data, the red solid line shows the corresponding BC relation. The dotted line shows the relation fitted to relaxed clusters (blue data) and dashed line to merging clusters (red data). The dot–dashed and long dashed lines shows relations fitted independently to each survey and the red dashed line is the best-fitting uncorrected relation from Leauthaud et al. (2010). Errors on data indicate statistical uncertainties.

measured with *Chandra*. We modified our temperatures using the best-fitting relations for the full energy band by equation (3). and table 2 in Schellenberger et al. (2015). For CFHTLS and COSMOS which are measured with pn only, we used the ACIS–pn relation. For CCCP which uses all three *XMM*-EPIC detectors (pn, MOS1 and MOS2), we used the values for ACIS-combined *XMM*.

Nevalainen et al. (2010) found that *Chandra* results on average in ~2 per cent higher fluxes in the soft energy band (0.5–2.0 keV) and ~11 per cent higher in the hard band (2.0–7.0 keV) than pn. As fluxes are directly related to luminosity, any discrepancy in measured fluxes applies directly to luminosities. Mahdavi et al. (2013) reported ~3 per cent higher bolometric luminosities for *Chandra* than for combined *XMM*. As we measure luminosities in a 0.1–2.4 keV band, we increased our *XMM*-based luminosities by 2 per cent in order to match the *Chandra* calibration.

The best-fitting parameters of the scaling relations fitted to our modified *XMM* data are given in Table 3, and show the relations in Figs 16–18. As expected from the small modification to luminosities, we find that modifying luminosities does not affect the resulting relations. However, modifying temperatures drives the slopes of the L_X–T_X and M_{500}–T_X relations to flatter values. The flattening of the slopes of the bias-corrected L_X–T_X and M_{500}–T_X relations are 0.35 ± 0.16 and 0.23 ± 0.15, respectively.

5 DISCUSSION

Measurements of a large number of clusters from a wide mass range are needed to gain precise constraints on scaling relations. A large spread in mass improves the constraint on the slope of the scaling and as lensing mass measurements have an intrinsic scatter of ~20–30 per cent (e.g. Becker & Kravtsov 2011), several systems in each mass range and a good understanding of systematic uncertainties and observational biases are needed to accurately recover the average relation.

With the inclusion of the 12 low-mass clusters analysed in this work, we have more than doubled the number of systems at low and intermediate masses available in the sample used for lensing
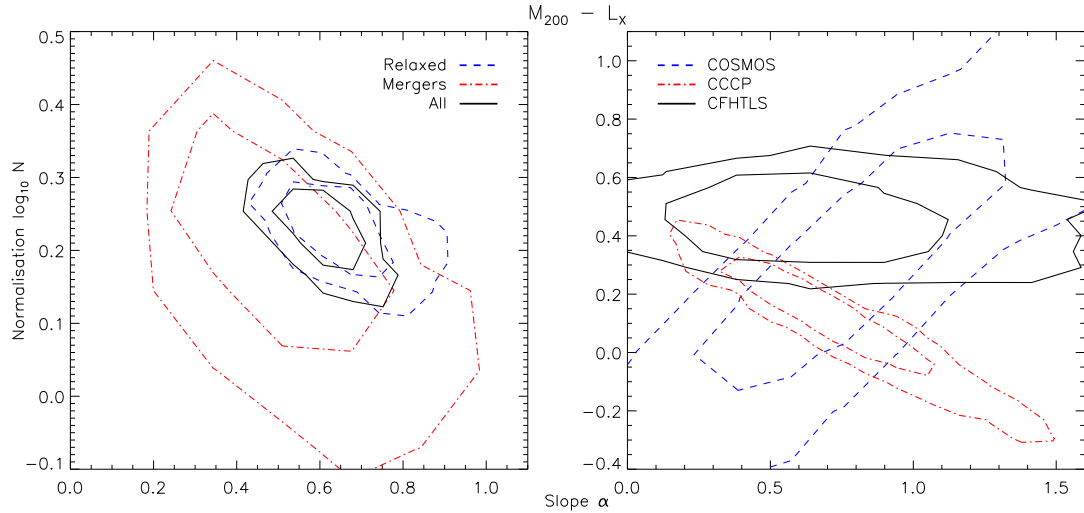
Figure 11. Confidence contours for the posterior distributions of slope and normalization at 68 and 95 per cent significance for the M_{200}–L_X relations fitted to each respective subsample.
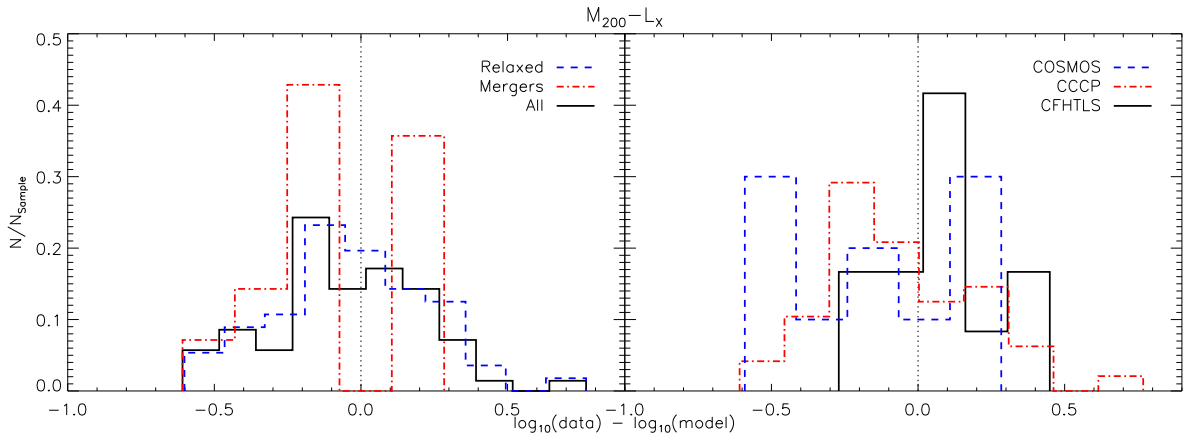

Figure 12. The distribution of residuals for each subsample with respect to the M_{200}–L_X relation fitted to the full sample. N_{Sample} is defined as the number of systems in each subsample.
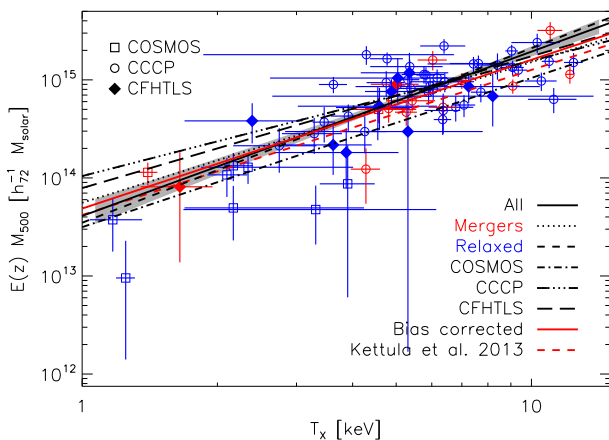

Figure 13. The scaling of mass M_{500} to core-excised temperature T_X. The black solid line and grey shaded region shows the best-fitting relation and statistical uncertainty fitted to all data, the red solid line shows the corresponding BC relation. The dotted line shows the relation fitted to relaxed clusters (blue data) and dashed line to merging clusters (red data). The dot–dashed and long dashed lines shows relations fitted independently to each survey and the red dashed line is the best-fitting uncorrected relation from Kettula et al. (2013b). Errors on data indicate statistical uncertainties.

calibrated scaling relations. Previously the only individual low-mass systems with lensing and X-ray measurements were 10 groups from the COSMOS field, which extend to a larger redshift and thus possibly affected by evolutionary effects (e.g. Jee et al. 2011). On the other hand, there are extensive recent and ongoing observational efforts to obtain mass calibration for massive clusters by e.g. LoCuSS (Okabe et al. 2010), CCCP (Mahdavi et al. 2013) and Weighing the Giants (WtG; von der Linden et al. 2014a).

The systems analysed in this work increase the statistical power of the low-mass end and thus improve the precision of the constraint. In addition, we include a correction for Eddington bias. This renders our sample ideal to study mass-dependent effects and deviations from self-similar scaling.

5.1 Bias correction

As the Eddington bias correction affects the slope of the relation, it is important in order to understand possibly mass-dependent deviations from self-similarity. In addition to affecting the slope, the bias correction results in a decrease in scatter, which indicates a strong covariance between the X-ray selection and lensing mass. The decreased scatter is an effect of the mass dependence of the
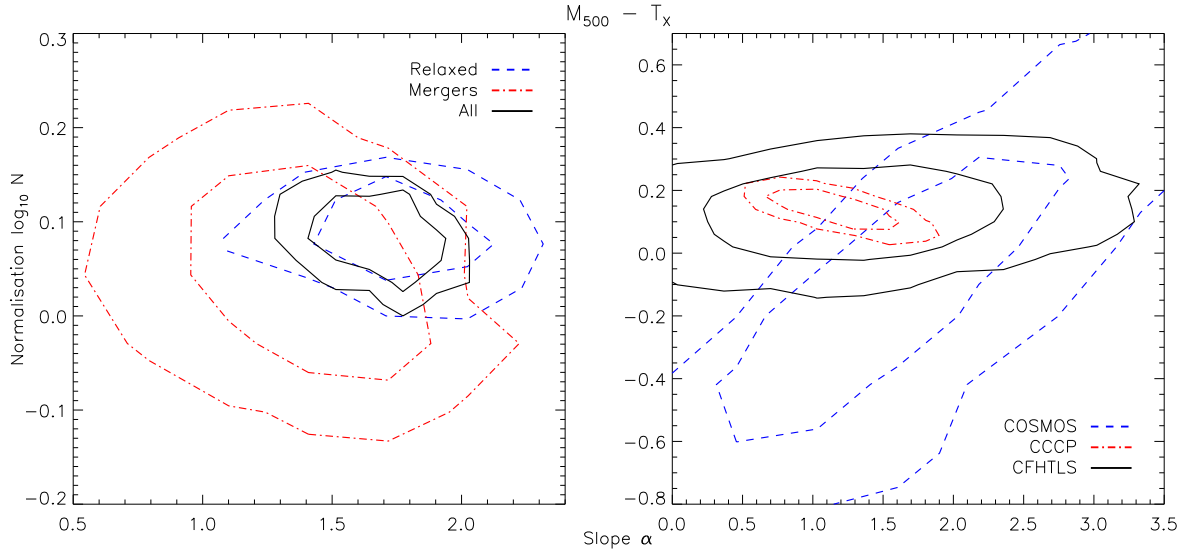
Figure 14. Confidence contours for the posterior distributions of slope and normalization at 68 and 95 per cent significance for the M_{500}–T_X relations fitted to each respective subsample.
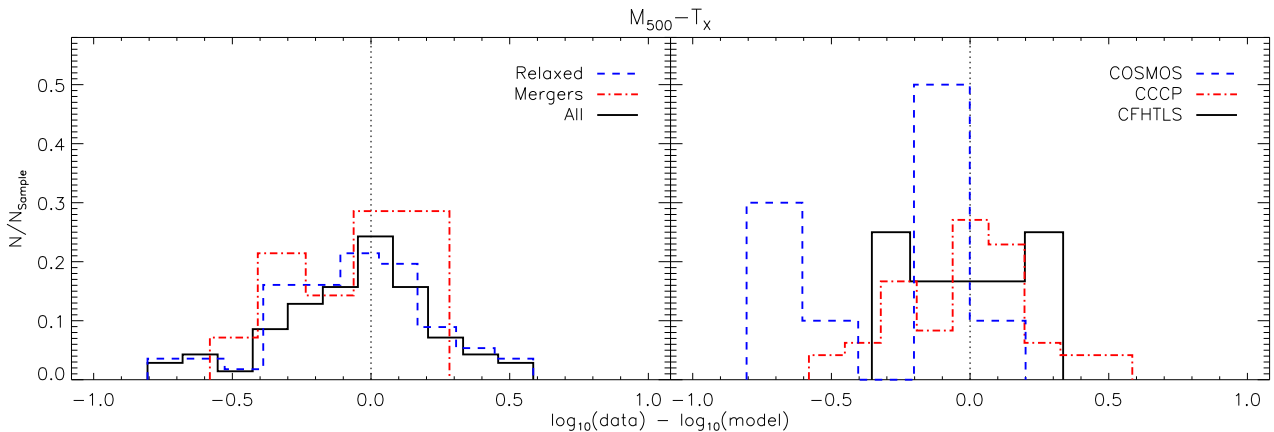

Figure 15. The distribution of residuals for each subsample with respect to the M_{500}–T_X relation fitted to the full sample. N_{Sample} is defined as the number of systems in each subsample.

bias correction, which drives preferentially upscattered high-mass systems towards the mean relation. As the strength of the bias correction depends on sample selection and the covariance between the selection and the parameter of interest, it is important to note that the effects of the corrections differ between different surveys.

As Eddington bias arises as a consequence of intrinsic scatter and an exponential drop in the population, i.e. the high-mass decline of the mass function, it will also affect cluster simulations incorporating a realistic treatment of the intrinsic scatter about the mean relation. Therefore we want to stress the importance of applying the bias correction for simulated cluster populations which are compared to our BC relations. A full cosmological modelling of cluster core-excised L_X or T_X function should include a convolution of the cluster mass function and BC scaling relation with a lognormal distribution describing the scatter term about the mean relation.

5.2 Sensitivity to high-mass sample

In order to test the sensitivity of the global relations to the sample, we replace CCCP with a different high-mass sample. We construct

the new sample by correlating the *Chandra* and *ROSAT* X-ray measurements of the X-ray selected sample presented in Mantz et al. (2010) with the compilation of published weak lensing mass measurements by Sereno (2014). We find 42 clusters with core-excised temperatures, core-excised soft band X-ray luminosities and weak lensing masses. We refer to this sample as the literature high-mass sample and present the measurements in Appendix C. The lensing masses are from various sources and consequently suffer from different uncertainties.

As 36 of the clusters in the literature sample have temperatures measured with *Chandra* and six with *ASCA*, we assume the calibration of the sample to match that of *Chandra*. We fit L_X–T_X, M–L_X and M–T_X relations to a sample consisting of the literature sample and COSMOS and CFHTLS data modified to match *Chandra* calibration (see Table 4). We also apply Eddington bias corrections to this sample and fit BC relations. We show the data and relations and compare them to the corresponding relations using CCCP converted to *Chandra* calibration as the high-mass sample in Figs 16–18. The literature high-mass sample results in systematically steeper relations with lower scatter than CCCP. We also fitted the relations

Table 3. The fit parameters and intrinsic scatter with the corresponding statistical uncertainties of the scaling relations with *XMM* temperatures and luminosities modified to match *Chandra* calibration.

	α	$\log_{10}N$	$\sigma_{\log(A|B)}$
L_X–T_X *Chandra* calibration			
All data	$2.25^{+0.15}_{-0.15}$	$0.02^{+0.04}_{-0.04}$	$0.20^{+0.04}_{-0.03}$
Bias corrected	$2.17^{+0.15}_{-0.13}$	$-0.01^{+0.03}_{-0.03}$	$0.13^{+0.04}_{-0.04}$
M_{200}–L_X *Chandra* calibration			
All data	$0.72^{+0.08}_{-0.07}$	$0.31^{+0.04}_{-0.04}$	$0.15^{+0.03}_{-0.03}$
Bias corrected	$1.29^{+0.14}_{-0.13}$	$-0.07^{+0.03}_{-0.03}$	$0.08^{+0.04}_{-0.04}$
M_{500}–T_X *Chandra* calibration			
All data	$1.44^{+0.15}_{-0.15}$	$-0.05^{+0.04}_{-0.04}$	$0.16^{+0.03}_{-0.03}$
Bias corrected	$1.29^{+0.14}_{-0.13}$	$-0.07^{+0.03}_{-0.03}$	$0.08^{+0.04}_{-0.04}$

Notes. α is the slope of the relation, $\log_{10}N$ the normalization and $\sigma_{\log(A|B)}$ the intrinsic scatter. BC relations are fitted to the full data set.
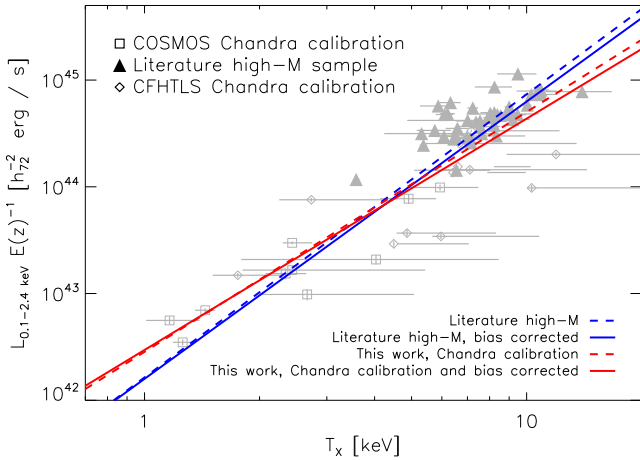

Figure 16. Comparison of L_X–T_X relations using different high-mass samples, blue lines show relations using the literature sample, red lines using CCCP converted to *Chandra* calibration. Solid lines show the BC relations, dashed lines the uncorrected lines. The high-mass samples are combined with COSMOS and CFHTLS data converted to *Chandra* calibration. COSMOS and CFHTLS data converted to *Chandra* calibration and measurements of the literature high-mass sample are shown in grey.

Figure 17. Comparison of M–L_X relations using different high-mass samples, blue lines show relations using the literature sample, red lines using CCCP converted to *Chandra* calibration. Solid lines show the BC relations, dashed lines the uncorrected lines. The high-mass samples are combined with COSMOS and CFHTLS data converted to *Chandra* calibration. COSMOS and CFHTLS data converted to *Chandra* calibration and measurements of the literature high-mass sample are shown in grey.

Figure 18. Comparison of M–T_X relations using different high-mass samples, blue lines show relations using the literature sample, red lines using CCCP converted to *Chandra* calibration. Solid lines show the BC relations, dashed lines the uncorrected lines. The high-mass samples are combined with COSMOS and CFHTLS data converted to *Chandra* calibration. COSMOS and CFHTLS data converted to *Chandra* calibration and measurements of the literature high-mass sample are shown in grey.

using a subset of the literature sample consisting only of WtG and CLASH clusters with lensing measurements from Applegate et al. (2014) and Umetsu et al. (2014), but found that this had a very small effect.

Based on the reported cross-calibration discrepancies, we expect flatter L_X–T_X and M–T_X relations for the *Chandra*-based literature sample than for our observed uncorrected *XMM* data (as demonstrated in Section 4.5). For M–L_X relation, we both expect and find consistent relations, demonstrating consistency in mass and L_X measurements. However, in case of the L_X–T_X and M–T_X relations, we find that slopes obtained using the literature sample matches the uncorrected *XMM*-based relations using CCCP, which are steeper than the relations corrected for *Chandra* calibration. This demonstrates some tension in the X-ray temperatures of the high-mass samples. One possible source of uncertainty is that we use the
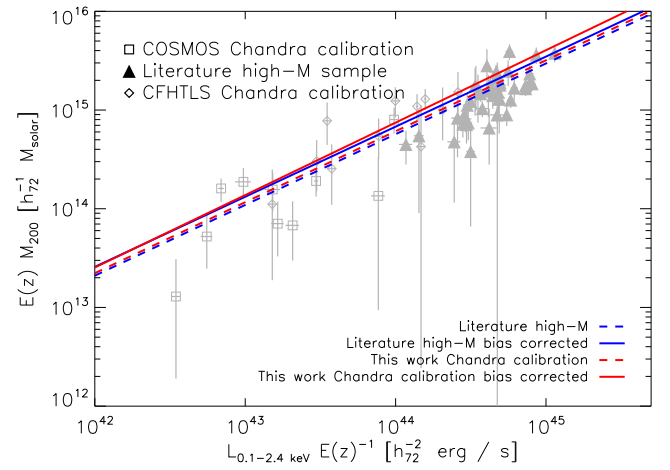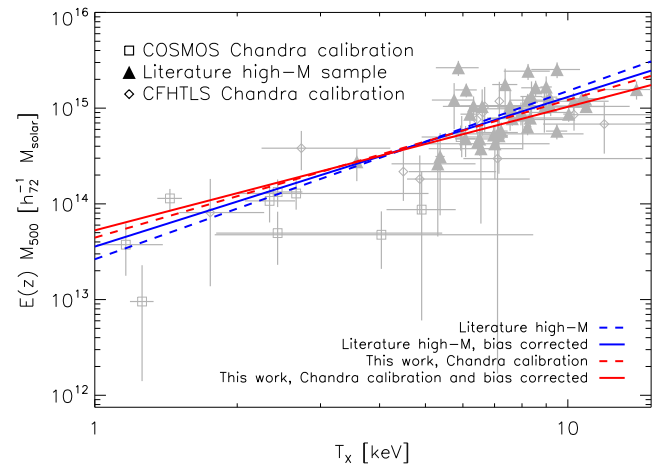
locally calibrated relation of Schellenberger et al. (2015) to convert our *XMM*-based temperatures to match *Chandra* calibration.

Overall, this shows that even after proper accounting for observational biases and considering X-ray cross-calibration issues, differences between samples persist. This variance between samples is still the dominant effect leading to discrepant scaling relations.

5.3 Mass dependence

We fit scaling relations independently to each of the three surveys making up our sample and use them as approximate mass bins in order to attempt to study the mass dependence of the scaling relations. Unfortunately, the statistical uncertainties of the relations

Table 4. The M–L_X relation after replacing CCCP data with the literature sample from Mantz et al. (2010) and Sereno (2014) to check the sensitivity of the scaling relations.

	α	$\log_{10}N$	$\sigma_{\log(A|B)}$
L_X–T_X literature high-mass sample			
All data	$2.65^{+0.18}_{-0.18}$	$0.07^{+0.04}_{-0.04}$	$0.18^{+0.04}_{-0.04}$
Bias corrected	$2.60^{+0.10}_{-0.13}$	$0.02^{+0.03}_{-0.05}$	$0.09^{+0.05}_{-0.04}$
M_{200}–L_X literature high-mass sample			
All data	$0.72^{+0.07}_{-0.06}$	$0.28^{+0.04}_{-0.04}$	$0.08^{+0.04}_{-0.04}$
Bias corrected	$0.71^{+0.08}_{-0.08}$	$0.35^{+0.03}_{-0.03}$	$0.07^{+0.03}_{-0.03}$
M_{500}–T_X literature high-mass sample			
All data	$1.76^{+0.19}_{-0.18}$	$-0.05^{+0.04}_{-0.04}$	$0.15^{+0.03}_{-0.03}$
Bias corrected	$1.56^{+0.19}_{-0.17}$	$-0.05^{+0.03}_{-0.03}$	$0.07^{+0.03}_{-0.03}$

Notes. α is the slope of the relation, $\log_{10}N$ the normalization and $\sigma_{\log(A|B)}$ the intrinsic scatter. The relations are fitted to a combination of COSMOS and CFHTLS data corrected to match *Chandra* calibration and the literature high-mass sample.

fitted to the low-mass COSMOS and intermediate-mass CFHTLS subsamples are large due to the small number of systems and the relatively small mass range. The constraints for the high-mass CCCP subsample are better due to the larger number of systems in the CCCP sample. The relations are described in Figs 7–9, 10–12 and 13–15, and Table 2. We also experimented with CCCP only relations with masses measured assuming the mass–concentration relation of Dutton & Macciò (2014) instead of Duffy et al. (2008), but find no difference in the best-fitting parameters.

For COSMOS, we detect a trend for a larger scatter in mass than the higher mass CFHTLS and COSMOS subsamples. For the M–L_X relation, CFHTLS results in higher normalizations than CCCP, whereas the normalization of the CCCP only L_X–T_X is significantly higher than for COSMOS and CFHTLS. As CCCP selection is based on both L_X and T_X, the CCCP only L_X–T_X is susceptible to residual scatter affecting the CCCP L_X (see Section 4.1.1). This could result in the normalization being biased high.

We measure residuals (defined as the ratio of data to model prediction) to the BC relations as a function of luminosity and temperature in Fig. 19. We stack the residuals using three mass bins by calculating the median and median standard deviation of the residual in

each bin (see Table 5). Here, a mass-dependent deviation from the main relation would drive the median residual away from unity. We use the best-fitting relations to determine the luminosity or temperature corresponding to the mass limits of each bin and include the systems falling into the luminosity or temperature range in the stack (here we assume $M_{500} = 0.65\,M_{200}$). We also repeat the analysis for the BC relation using the literature high-mass sample (Table 5).

For M–L_X and M–T_X relations where we perform full bias corrections, we find consistent behaviour using both data sets, whereas there is tension for the L_X–T_X relation. The M–L_X and M–T_X residuals show that low-mass systems ($M_{200} < 2 \times 10^{14}\,M_\odot$) tend to be below the best-fitting relation, intermediate mass systems ($M_{200} = 2$–$8 \times 10^{14}\,M_\odot$) above the mean relation and high-mass systems ($M_{200} > 2 \times 10^{14}\,M_\odot$) above or at the best-fitting relation. This is consistent with a mass-dependent scaling where low-mass objects follow a steeper scaling than high-mass objects, with the effect being stronger for the mass–luminosity relation than for the mass–temperature relation. This implies that galaxy groups are warmer and more luminous for their mass than clusters. We also see a tendency for steepening at low masses in the L_X–T_X relation using CCCP, whereas the literature high-mass sample would result in opposite behaviour.

The strong indications of a mass dependence in the M–L_X and M–T_X relations show that there is a need to explore more complicated scaling relation than a single power-law arising from self-similar theory. However, due to the lack of theoretical priors for the functional form and large uncertainties of the data, we do not attempt to model a more complicated scaling. The inferred mass dependence can be attributed to the inclusion of intermediate-mass CFHTLS data and proper accounting for observational biases. Indeed, in Kettula et al. (2013b) we studied the scaling of lensing mass to temperature of COSMOS groups and clusters from 160SD and CCCP (with different M and T_X measurements than here), and found a single relation connecting groups and high-mass clusters.

Several previous studies have shown that the scaling relation can deviate from the purely gravitational self-similar prediction and that the deviations become stronger for low-mass systems with masses below a few times $10^{14}\,M_\odot$ (see e.g. Giodini et al. 2013, and references therein). However, these studies relied on possibly biased HSE mass estimates and this work gives the first indications of different scaling for groups and clusters using accurate lensing masses.
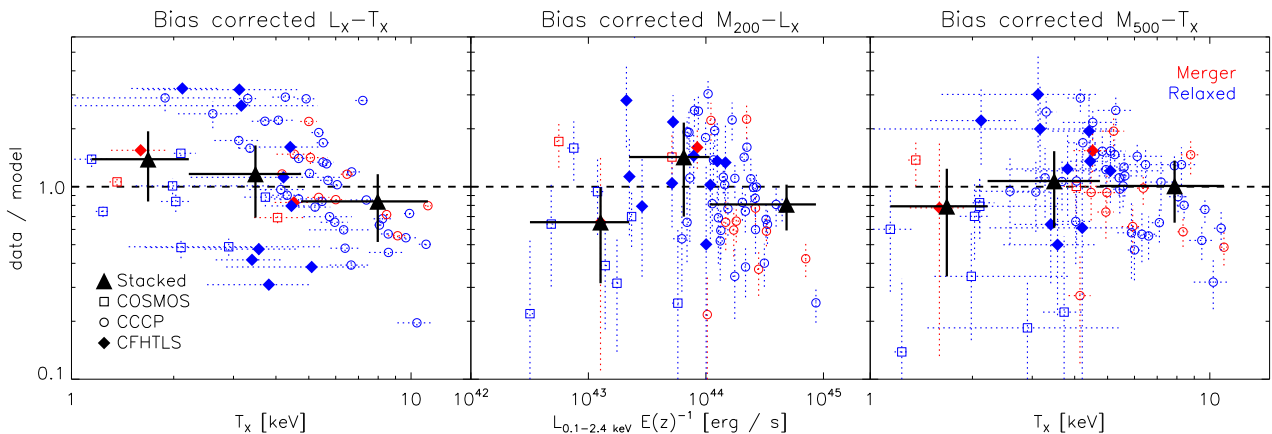
Figure 19. Residuals (defined as the ratio of data to model prediction) for the Eddington bias-corrected L_X–T_X (left-hand panel), M–L_X (middle panel) and M–T_X relations. Blue and red dotted data shows the residuals for individual merging and relaxed systems, squares indicate systems from COSMOS, circles from CCCP and solid diamonds from CFHTLS. Large triangles show the median and median standard deviation of stacked residuals for three mass bins.

Table 5. Stacked residuals of the BC relations.

	$M_{200} < 2 \times 10^{14}$ M$_\odot$ Stacked data/model	$M_{200} = 2–8 \times 10^{14}$ M$_\odot$ Stacked data/model	$M_{200} > 8 \times 10^{14}$ M$_\odot$ Stacked data/model
L_X–T_X this work	1.39 ± 0.55	1.16 ± 0.47	0.84 ± 0.32
L_X–T_X literature high-mass sample	1.33 ± 0.53	0.73 ± 0.49	0.93 ± 0.21
M_{200}–L_X this work	0.65 ± 0.34	1.42 ± 0.73	0.81 ± 0.22
M_{200}–L_X literature high-mass sample	0.73 ± 0.40	1.11 ± 0.45	0.93 ± 0.29
M_{500}–T_X this work	0.79 ± 0.45	1.07 ± 0.46	1.00 ± 0.36
M_{500}–T_X literature high-mass sample	0.89 ± 0.11	1.12 ± 0.65	0.85 ± 0.22

Notes. This work refers to relations combining COSMOS, CFHTLS and CCCP data, literature high-mass sample to relations combining COSMOS and CFHTLS data corrected to match *Chandra* calibration with the literature high-mass sample.

As shown by Fig. 1 and e.g. Giodini et al. (2010), the AGN contribution to the energetics of the intracluster gas increases with decreasing mass. As baryonic feedback becomes significant for galaxy groups, energy injection to the intracluster gas in galaxy groups can lead to different scaling for low-mass systems, as indicated in recent simulations by Planelles et al. (2014), Le Brun et al. (2014) and Pike et al. (2014).

Energy injection to the intracluster gas in galaxy groups may also contribute to HSE mass bias in groups. Indeed, in Kettula et al. (2013b) we report an HSE mass bias increasing with decreasing mass. This is to be contrasted to the analytical model for non-thermal pressure in galaxy clusters by Shi & Komatsu (2014), who infer an HSE mass bias due to turbulence in the intracluster medium which increases with increasing mass, in line with direct lensing measurements reported in Mahdavi et al. (2013), von der Linden et al. (2014b) and Israel et al. (2015). However, the model of Shi & Komatsu (2014) is contradicted by recent simulations (Miniati 2015 and Miniati, private communication), who shows that the turbulence scales with thermal energy and should thus result in an HSE mass bias which is constant in mass. As the non-thermal contribution from AGN becomes significant at group levels, the Miniati simulations would thus result in an HSE mass bias consistent with Kettula et al. (2013b).

Finally, X-ray line emission on group scales may contribute to a break in the mass-to-luminosity relation. Typically the shape of the X-ray spectra of clusters is determined by the bremsstrahlung continuum, but at group masses line emission due to metallicity becomes significant. This results in an extra emission component on top of the bremsstrahlung responsible for > 50 per cent of the total X-ray emission, making groups more luminous for their mass. This is not accounted for by the self-similar model and is qualitatively consistent with our findings above.

5.4 Effects of substructure and triaxiality

Simulations by e.g. Meneghetti et al. (2010) and Becker & Kravtsov (2011) indicate that weak lensing masses obtained by fitting an NFW profiles to tangential shear profiles suffer from a scatter of $\sim$20–25 per cent (see also discussion in Sereno & Ettori 2014). The main source for the scatter and bias are triaxiality and cluster substructure. Triaxiality and substructure may also bias the resulting masses low by $\sim$5 per cent. As merging clusters per definition display on average stronger deviations from spherical symmetry than relaxed clusters, we expect them to be more strongly affected by scatter and possible bias related to triaxiality and substructure. The large size of the sample allows us to construct subsamples of relaxed

and merging clusters to study this effect. We fit relations to the relaxed and merging subsample, and describe them in Figs 7–9, 10–12 and 13–15, and Table 2.

In the case of the bias-corrected M–L_X and M–T_X relations, which are affected by biases and scatter in lensing masses, we see a trend for a larger scatter in the merging subsample, albeit at a low statistical significance. We do not find any significant differences in the parameters (see Figs 11 and 14), but note that the relaxed subsample seems to favour steeper slopes than the merging subsample. This could be evidence for some residual bias originating from the cool core (see Section 2.2). We also note that possible biases in the slopes do not affect the scatters (Vikhlinin et al. 2009).

For the L_X–T_X relation, which is unaffected by lensing masses, we see the opposite trend in scatter, i.e. mergers have a lower scatter (see Table 2). Once again we find no significant difference in the parameters between merging and relaxed clusters (Fig. 8), but note that merging clusters might favour a steeper slope and higher normalization. This is supported by Bharadwaj et al. (2015), who find a steeper slope and higher normalization for the L_X–T_X relation of preferentially relaxed strong cool core groups. However, as Bharadwaj et al. (2015) used non-core-excised bolometric luminosities, their trend is most likely driven by the inclusion of bright cool cores.

We test how strongly the above effects are related to uncertainties arising from assuming an NFW profile by comparing the mass residuals of the M–T_X relation using 11 merging CCCP clusters with mass measurements determined with the NFW assumption and aperture densitometry, available from Hoekstra et al. (2015). Aperture mass relates shear directly to projected density contrast, without any assumptions of geometry. A change in bias would move the residuals systematically to one direction, whereas scatter is determined from the spread of the distribution. We find no difference in scatter or bias using the two mass measurement methods (see Fig. 20).

Overall, mergers contribute little to the total scatter for X-ray selected samples such as ours. Our measurements also demonstrate that the intrinsic scatter in temperature at fixed mass is significantly lower than in the luminosity at fixed mass. This shows that temperature is a good low-scatter mass proxy for cluster samples selected on X-ray brightness. However, samples dominated by merging clusters, such as Planck Collaboration XXIX (2013), might have less scatter using other proxies such as gas mass M_{gas} or thermal energy content of the intracluster gas $Y_X = T_X \times M_{gas}$. Mahdavi et al. (2013) studied these proxies using the high-mass CCCP sample and found that while M_{gas} has lower scatter, Y_X is independent of cluster morphology.
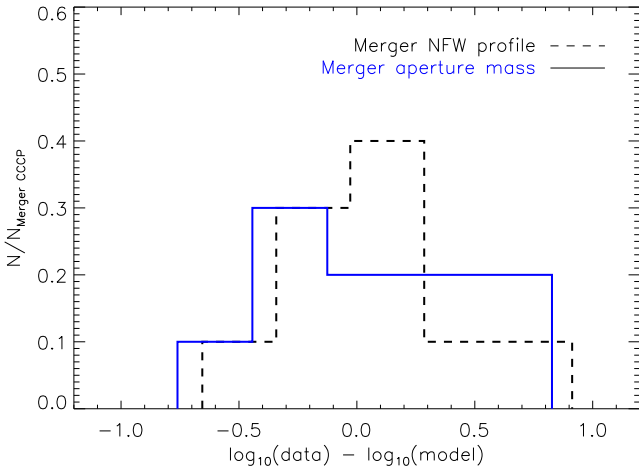
Figure 20. The mass residuals in the mass–temperature relation for merging CCCP clusters. We show the residuals of M_{500} for all merging CCCP clusters measured using an NFW density profile (dashed black line) and aperture mass (blue solid line) to the best-fitting M–T_X relation fitted to all merging clusters in the total sample.

6 SUMMARY AND CONCLUSIONS

We performed weak lensing and X-ray analysis for a sample of 12 individual low-mass clusters within the context of the CFHTLenS and *XMM*-CFHTLS surveys. This work extends our previous work by inclusion of measurements of intermediate mass systems and provides the first M–L_X relation for low-mass systems with individual lensing mass measurements. We find X-ray luminosities between a few times 10^{43} erg s^{-1} and a few times 10^{45} erg s^{-1}, temperatures ranging from $\sim$2–7 keV and masses M_{200} of $\sim 10^{14}$–10^{15} M$_\odot$.

Combining the systems analysed in this work with lower mass COSMOS and higher mass CCCP systems from the literature, we end up with a sample of 70 systems, spanning over two orders of magnitude in mass, three orders of magnitude in luminosity and roughly one order of magnitude in temperature.

We present a correction for Eddington bias and also apply a Malmquist bias correction for the independent variable (x-direction). As our samples are X-ray selected, we are able to provide fully bias-corrected M–L_X and M–T_X relations. By quoting the relations and intrinsic scatters of the parameters, we provide the current limitations for X-ray luminosity and temperature as cluster mass proxies. We find that the scatter in T_X at fixed mass is significantly lower than that of L_X. Though observationally more expensive than L_X, this feature renders T_X an attractive mass proxy for use in cosmological work.

We use the three surveys making up the sample as overlapping mass bins to study mass-dependent effects. As the relations fitted to individual surveys suffer from large statistical uncertainties, we do not find any statistically significant effects. Inspecting residuals for the BC relations, we see for the first time indications that galaxy groups are more luminous and warmer for their mass than clusters using accurate lensing masses, implying a steepening in the scaling relations. We expect this steepening to be stronger for luminosity than for temperature. A steepening implies the need for a more complicated scaling than a single power-law predicted from the purely gravitational self-similar model.

We construct a high-mass sample from the literature to investigate the sensitivity of the relations to the sample. Even after accounting for observational biases and X-ray cross-calibration issues,

the literature sample leads to steeper L_X–T_X and M–T_X relations, demonstrating that variance between samples is the dominant effect leading to discrepant scaling. However, the inferred mass dependence of the relations is also present with the literature high-mass sample.

We divide the sample into subsamples of relaxed and merging clusters based on the offset between the X-ray peak and the BCG to investigate the morphology dependence of the scaling. For M–L_X and M–T_X relations which include lensing masses, we find that mergers may result in enhanced scatter, which we attribute to cluster triaxiality and substructure. For the L_X–T_X relation which is independent of lensing measurements, we find the opposite trend in scatter. We study if using aperture mass measurements instead of assuming an NFW profile improves the mass measurements for merging systems, but find no significant effect. For the overall relations fitted to the full sample, we find that mergers contribute little. However, for samples dominated by merging systems, lensing mass calibration using other methods than a single NFW profile may lead to improved mass calibration.

We also explore the effects of X-ray cross-calibration and provide scaling relations with our *XMM–Newton*-based temperatures and luminosities converted to match *Chandra* calibration. We find that *Chandra* calibration leads to flatter slopes for L_X–T_X and M–T_X relations, whereas the M–L_X relation is unaffected.

In conclusion, our work provides a correction for Eddington bias and fully BC scaling relations over a large mass range. We demonstrate the importance of having well-understood samples on all mass scales and a better understanding of the covariances between selection and observables. We detect the first indications of mass dependent scaling relations using weak lensing masses and demonstrate the need for more observations of low-mass systems in order to accurately measure the inferred mass dependence.

Author Contributions: All authors contributed to the development and writing of this paper. The authorship list reflects the lead authors of this paper (KK, SG, EvU, HH, AF, ML) followed by two alphabetical groups. The first alphabetical group includes key contributors to the science analysis and interpretation in this paper, the founding core team and those whose long-term significant effort produced the final CFHTLenS and *XMM*-CFHTLS data products. The second group covers members of the CFHTLenS and *XMM*-CFHTLS team who made a significant contribution to the project.

REFERENCES

Allevato V. et al., 2012, ApJ, 758, 47
Applegate D. E. et al., 2014, MNRAS, 439, 48
Bartelmann M., 1996, A&A, 313, 697
Becker M. R., Kravtsov A. V., 2011, ApJ, 740, 25
Benítez N., 2000, ApJ, 536, 571
Benjamin J. et al., 2013, MNRAS, 431, 1547
Bharadwaj V., Reiprich T. H., Lovisari L., Eckmiller H. J., 2015, A&A, 573, A75
Böhringer H. et al., 2007, A&A, 469, 363
Connor T., Donahue M., Sun M., Hoekstra H., Mahdavi A., Conselice C. J., McNamara B., 2014, ApJ, 794, 48
Corless V. L., King L. J., 2007, MNRAS, 380, 149
Cypriano E. S., Sodré L., Jr, Kneib J.-P., Campusano L. E., 2004, ApJ, 613, 95
Dahle H., 2006, ApJ, 653, 954
Donahue M. et al., 2014, ApJ, 794, 136
Duffy A. R., Schaye J., Kay S. T., Dalla Vecchia C., 2008, MNRAS, 390, L64
Dutton A. A., Macciò A. V., 2014, MNRAS, 441, 3359
Eckmiller H. J., Hudson D. S., Reiprich T. H., 2011, A&A, 535, A105
Eddington A. S., 1913, MNRAS, 73, 359
Erben T. et al., 2013, MNRAS, 433, 2545
Fabjan D., Borgani S., Rasia E., Bonafede A., Dolag K., Murante G., Tornatore L., 2011, MNRAS, 416, 801
Finoguenov A., Böhringer H., Zhang Y.-Y., 2005, A&A, 442, 827
Ford J. et al., 2012, ApJ, 754, 143
Ford J. et al., 2015, MNRAS, 447, 1304
Giodini S. et al., 2010, ApJ, 714, 218
Giodini S., Lovisari L., Pointecouteau E., Ettori S., Reiprich T. H., Hoekstra H., 2013, Space Sci. Rev., 177, 247
Gozaliasl G. et al., 2014, A&A, 566, A140
Hamana T., Takada M., Yoshida N., 2004, MNRAS, 350, 893
Heymans C. et al., 2012, MNRAS, 427, 146
Heymans C. et al., 2013, MNRAS, 432, 2433
Hildebrandt H. et al., 2012, MNRAS, 421, 2355
Hoekstra H., 2001, A&A, 370, 743
Hoekstra H., Hartlap J., Hilbert S., van Uitert E., 2011, MNRAS, 412, 2095
Hoekstra H., Mahdavi A., Babul A., Bildfell C., 2012, MNRAS, 427, 1298
Hoekstra H., Bartelmann M., Dahle H., Israel H., Limousin M., Meneghetti M., 2013, Space Sci. Rev., 177, 75
Hoekstra H., Herbonnet R., Muzzin A., Babul A., Mahdavi A., Viola M., Cacciato M., 2015, MNRAS, 449, 685
Horner D. J., 2001, PhD thesis, Univ. Maryland, College Park
Hudson D. S., Mittal R., Reiprich T. H., Nulsen P. E. J., Andernach H., Sarazin C. L., 2010, A&A, 513, A37
Hudson M. J. et al., 2015, MNRAS, 447, 298
Israel H., Reiprich T. H., Erben T., Massey R. J., Sarazin C. L., Schneider P., Vikhlinin A., 2014, A&A, 564, A129
Israel H., Schellenberger G., Nevalainen J., Massey R., Reiprich T., 2015, MNRAS, 448, 814
Jee M. J. et al., 2011, ApJ, 737, 59
Kaiser N., 1986, MNRAS, 222, 323
Kelly B. C., 2007, ApJ, 665, 1489
Kettula K., Nevalainen J., Miller E. D., 2013a, A&A, 552, A47
Kettula K. et al., 2013b, ApJ, 778, 74
Kilbinger M. et al., 2013, MNRAS, 430, 2200
Kitching T. D. et al., 2014, MNRAS, 442, 1326
Kubo J. M. et al., 2009, ApJ, 702, L110
Le Brun A. M. C., McCarthy I. G., Schaye J., Ponman T. J., 2014, MNRAS, 441, 1270
Leauthaud A. et al., 2010, ApJ, 709, 97
Lovisari L., Reiprich T., Schellenberger G., 2015, A&A, 573, A118
McCarthy I. G. et al., 2010, MNRAS, 406, 822
Mahdavi A., Hoekstra H., Babul A., Henry J. P., 2008, MNRAS, 384, 1567
Mahdavi A., Hoekstra H., Babul A., Bildfell C., Jeltema T., Henry J. P., 2013, ApJ, 767, 116
Mahdavi A., Hoekstra H., Babul A., Bildfell C., Jeltema T., Henry J. P., 2014, ApJ, 794, 175
Mantz A., Allen S. W., Ebeling H., Rapetti D., Drlica-Wagner A., 2010, MNRAS, 406, 1773
Mantz A. B. et al., 2015, MNRAS, 446, 2205
Meneghetti M., Rasia E., Merten J., Bellagamba F., Ettori S., Mazzotta P., Dolag K., Marri S., 2010, A&A, 514, A93
Miller L., Kitching T. D., Heymans C., Heavens A. F., van Waerbeke L., 2007, MNRAS, 382, 315
Miller L. et al., 2013, MNRAS, 429, 2858
Miniati F., 2015, ApJ, 800, 60
Mirkazemi M. et al., 2015, ApJ, 799, 60
Nagai D., Kravtsov A. V., Vikhlinin A., 2007, ApJ, 668, 1
Navarro J. F., Frenk C. S., White S. D. M., 1997, ApJ, 490, 493
Nevalainen J., David L., Guainazzi M., 2010, A&A, 523, A22
Okabe N., Umetsu K., 2008, PASJ, 60, 345
Okabe N., Zhang Y.-Y., Finoguenov A., Takada M., Smith G. P., Umetsu K., Futamase T., 2010, ApJ, 721, 875
Okabe N. et al., 2014, PASJ, 66, 99
Pedersen K., Dahle H., 2007, ApJ, 667, 26
Pike S. R., Kay S. T., Newton R. D. A., Thomas P. A., Jenkins A., 2014, MNRAS, 445, 1774
Planck Collaboration XXIX, 2013, A&A, 571, A29
Planelles S., Borgani S., Fabjan D., Killedar M., Murante G., Granato G. L., Ragone-Figueroa C., Dolag K., 2014, MNRAS, 438, 195
Poole G. B., Babul A., McCarthy I. G., Fardal M. A., Bildfell C. J., Quinn T., Mahdavi A., 2007, MNRAS, 380, 437
Pratt G. W., Böhringer H., Croston J. H., Arnaud M., Borgani S., Finoguenov A., Temple R. F., 2007, A&A, 461, 71
Rasia E. et al., 2012, New J. Phys., 14, 055018
Read A. M., Guainazzi M., Sembay S., 2014, A&A, 564, A75
Rykoff E. S. et al., 2008, MNRAS, 387, L28
Schaye J. et al., 2010, MNRAS, 402, 1536
Schellenberger G., Reiprich T. H., Lovisari L., Nevalainen J., David L., 2015, A&A, 575, A30
Schmidt F., Leauthaud A., Massey R., Rhodes J., George M. R., Koekemoer A. M., Finoguenov A., Tanaka M., 2012, ApJ, 744, LL22
Scoville N. et al., 2007, ApJS, 172, 1
Semboloni E., Hoekstra H., Schaye J., van Daalen M. P., McCarthy I. G., 2011, MNRAS, 417, 2020
Semboloni E., Hoekstra H., Schaye J., 2013, MNRAS, 434, 148
Sereno M., 2014, preprint (arXiv:1409.5435)
Sereno M., Ettori S., 2014, preprint (arXiv:1407.7868)
Shaw L. D., Nagai D., Bhattacharya S., Lau E. T., 2010, ApJ, 725, 1452
Shi X., Komatsu E., 2014, MNRAS, 442, 521

Simpson F. et al., 2013, MNRAS, 429, 2249

Smith G. P., Kneib J.-P., Smail I., Mazzotta P., Ebeling H., Czoske O., 2005, MNRAS, 359, 417

Snowden S. L., Mushotzky R. F., Kuntz K. D., Davis D. S., 2008, A&A, 478, 615

Stanek R., Rasia E., Evrard A. E., Pearce F., Gazzola L., 2010, ApJ, 715, 1508

Sun M., Voit G. M., Donahue M., Jones C., Forman W., Vikhlinin A., 2009, ApJ, 693, 1142

Umetsu K. et al., 2009, ApJ, 694, 1643

Umetsu K., Broadhurst T., Zitrin A., Medezinski E., Hsu L.-Y., 2011, ApJ, 729, 127

Umetsu K. et al., 2014, ApJ, 795, 163

van Daalen M. P., Schaye J., Booth C. M., Dalla Vecchia C., 2011, MNRAS, 415, 3649

van den Bosch F. C., 2002, MNRAS, 331, 98

Velander M. et al., 2014, MNRAS, 437, 2111

Vikhlinin A. et al., 2009, ApJ, 692, 1033

Voges W. et al., 1999, A&A, 349, 389

von der Linden A. et al., 2014a, MNRAS, 439, 2

von der Linden A. et al., 2014b, MNRAS, 443, 1973

Wright C. O., Brainerd T. G., 2000, ApJ, 534, 34

Zhang Y.-Y., Andernach H., Caretta C. A., Reiprich T. H., Böhringer H., Puchwein E., Sijacki D., Girardi M., 2011, A&A, 526, A105

APPENDIX A: COSMOS AND CCCP LUMINOSITIES

The core-excised soft band luminosities for COSMOS are given in Table A1 and for CCCP in Table A2.

Table A1. The core-excised soft band X-ray luminosities of the COSMOS systems.

COSMOS xid	L_X 10^{43} erg s^{-1}
11	3.24 ± 0.11
17	1.81 ± 0.21
25	0.36 ± 0.02
29	1.14 ± 0.14
120	12.02 ± 1.27
149	0.72 ± 0.03
193	0.61 ± 0.05
220	14.38 ± 0.93
237	1.93 ± 0.18
262	2.42 ± 0.25

Table A2. The core-excised soft band X-ray luminosities of the CCCP systems.

Cluster name	L_X 10^{43} erg s^{-1}
3C295	19.24 ± 0.79
Abell0068	43.66 ± 1.63
Abell0115N	35.35 ± 0.70
Abell0115S	47.58 ± 1.52
Abell0209	55.94 ± 0.81
Abell0222	22.49 ± 1.16
Abell0223S	19.90 ± 0.69
Abell0267	30.85 ± 0.81
Abell0370	40.13 ± 1.39
Abell0383	21.17 ± 1.60
Abell0520	56.26 ± 1.22
Abell0521	53.48 ± 1.20
Abell0586	26.57 ± 1.16
Abell0611	30.51 ± 0.95
Abell0697	76.88 ± 1.80
Abell0851	36.15 ± 1.034
Abell0959	21.45 ± 1.72
Abell0963	43.14 ± 1.13
Abell1689	64.57 ± 0.45
Abell1763	60.15 ± 1.42
Abell1835	68.57 ± 0.52
Abell1914	64.83 ± 0.91
Abell1942	14.57 ± 0.70
Abell2104	66.88 ± 2.11
Abell2111	33.98 ± 2.50
Abell2163	159.92 ± 2.55
Abell2204	57.07 ± 0.42
Abell2218	37.63 ± 0.46
Abell2219	170.81 ± 1.66
Abell2259	24.87 ± 1.17
Abell2261	58.15 ± 3.22
Abell2390	118.57 ± 1.73
Abell2537	32.93 ± 1.23
CL0024.0+1652	8.87 ± 1.30
MACSJ0717.5+3745	137.73 ± 2.31
MACSJ0913.7+4056	26.79 ± 0.69
MS0015.9+1609	83.46 ± 2.10
MS0440.5+0204	9.15 ± 1.44
MS0451.6-0305	86.60 ± 2.66
MS0906.5+1110	28.08 ± 0.97
MS1008.1-1224	24.74 ± 1.22
MS1231.3+1542	14.30 ± 0.49
MS1358.1+6245	27.67 ± 1.60
MS1455.0+2232	30.35 ± 0.90
MS1512.4+3647	12.10 ± 1.10
MS1621.5+2640	27.71 ± 1.27
RXJ1347.5-1145	131.61 ± 2.01
RXJ1524.6+0957	16.93 ± 2.03

Table B1. The Eddington bias corrections for CFHTLS systems.

xid	$\frac{\mathrm{d}\alpha(ln(M))}{\mathrm{d}\ln(M)}$	M_{rat}	$T_{\mathrm{X, rat}}$	$L_{\mathrm{X, rat}}$
110090	0.988	0.915	0.939	0.763
110460	2.265	0.816	0.703	0.538
110850	1.410	0.881	0.887	0.681
110860	0.925	0.920	0.920	0.776
111180	2.220	0.819	0.903	0.547
210010	2.019	0.834	0.910	0.577
210020	0.576	0.949	0.968	0.854
210630	1.334	0.887	0.792	0.694
210740	1.792	0.851	0.830	0.613
210910	2.610	0.791	0.619	0.490
210970	3.042	0.761	0.824	0.437
102760	2.247	0.817	0.385	0.542

$\frac{\mathrm{d}\alpha(ln(M))}{\mathrm{d}\ln(M)}$ is the slope of the mass function, M_{rat}, $T_{\mathrm{X, rat}}$ and $L_{\mathrm{X, rat}}$ are the ratio of the Eddington BC mass, temperature and luminosity to the uncorrected values.

Table B2. The Eddington bias corrections for COSMOS systems.

xid	$\frac{\mathrm{d}\alpha(ln(M))}{\mathrm{d}\ln(M)}$	M_{rat}	$T_{\mathrm{X, rat}}$	$L_{\mathrm{X, rat}}$
11	0.806	0.930	0.967	0.803
17	0.797	0.931	0.966	0.800
25	0.235	0.979	0.990	0.937
29	0.857	0.926	0.898	0.787
120	0.959	0.917	0.954	0.766
149	0.699	0.939	0.972	0.826
193	0.436	0.961	0.979	0.8863
220	2.274	0.815	0.884	0.536
237	0.538	0.952	0.914	0.861
262	0.526	0.953	0.877	0.864

$\frac{\mathrm{d}\alpha(ln(M))}{\mathrm{d}\ln(M)}$ is the slope of the mass function, M_{rat}, $T_{\mathrm{X, rat}}$ and $L_{\mathrm{X, rat}}$ are the ratio of the Eddington BC mass, temperature and luminosity to the uncorrected values.

APPENDIX B: EDDINGTON BIAS CORRECTIONS

The Eddington bias corrections for CFHTLS, COSMOS and CCCP systems are given in Tables B1, B2 and B3, respectively.

APPENDIX C: LITERATURE HIGH-MASS SAMPLE

We give the X-ray luminosity and temperature measurements and lensing masses of the literature high-mass sample in Table C1. The Eddington bias corrections are described in Table C2.

Table B3. The Eddington bias corrections for CCCP systems.

Name	$\frac{\mathrm{d}\alpha(ln(M))}{\mathrm{d}\ln(M)}$	M_{rat}	$T_{\mathrm{X, rat}}$	$L_{\mathrm{X, rat}}$
3C295	2.7246	0.783	0.890	0.476
A68	2.3183	0.812	0.910	0.532
A115N	1.4342	0.879	0.945	0.677
A115S	1.5806	0.868	0.939	0.651
A209	1.7475	0.855	0.933	0.622
A222	1.5154	0.873	0.939	0.661
A223S	1.6967	0.859	0.930	0.630
A267	1.719	0.857	0.932	0.627
A370	4.2331	0.684	0.827	0.316
A383	1.3782	0.884	0.947	0.685
A520	2.423	0.805	0.910	0.518
A521	2.1272	0.826	0.920	0.561
A586	1.2077	0.897	0.947	0.720
A611	1.977	0.838	0.913	0.584
A697	2.5279	0.797	0.900	0.503
A851	3.5767	0.726	0.864	0.378
A959	3.0663	0.760	0.843	0.431
A963	2.1625	0.824	0.919	0.556
A1689	3.5814	0.725	0.871	0.378
A1763	2.6444	0.789	0.901	0.487
A1835	2.9783	0.766	0.888	0.445
A1914	2.2112	0.820	0.918	0.549
A1942	2.3255	0.812	0.910	0.530
A2104	2.3853	0.808	0.909	0.523
A2111	1.8756	0.845	0.917	0.598
A2163	2.6381	0.789	0.904	0.488
A2204	2.7131	0.784	0.899	0.479
A2218	2.4756	0.801	0.907	0.511
A2219	2.0995	0.829	0.921	0.566
A2259	1.6281	0.864	0.930	0.642
A2261	3.2946	0.744	0.871	0.407
A2390	3.1878	0.752	0.884	0.421
A2537	3.1944	0.751	0.823	0.419
CL0024	3.8042	0.711	0.367	0.341
MACS0717	5.6275	0.604	0.798	0.217
CL0910	1.8656	0.846	0.924	0.602
MS0016	4.8253	0.649	0.801	0.269
MS0440	1.0189	0.913	0.940	0.749
MS0451	3.6064	0.724	0.855	0.375
MS0906	2.1382	0.826	0.917	0.559
MS1008	2.7792	0.780	0.885	0.469
MS1231	0.78512	0.932	0.968	0.808
MS1358	2.5624	0.795	0.876	0.497
MS1455	2.355	0.810	0.912	0.527
MS1512	1.3264	0.888	0.936	0.694
MS1621	3.4511	0.734	0.849	0.390
RXJ1347	3.5424	0.728	0.870	0.382
RXJ1524	2.0217	0.834	0.890	0.569

$\frac{\mathrm{d}\alpha(ln(M))}{\mathrm{d}\ln(M)}$ is the slope of the mass function, M_{rat}, $T_{\mathrm{X, rat}}$ and $L_{\mathrm{X, rat}}$ are the ratio of the Eddington BC mass, temperature and luminosity to the uncorrected values.

Table C1. The literature high-mass sample from Mantz et al. (2010) and Sereno (2014).

Cluster name	z	L_X 10^{43} erg s^{-1}	T_X keV	kT ref.	M_{500} 10^{14} M$_\odot$	M_{200} 10^{14} M$_\odot$	Author code
Abell2029	0.0779	41.4 ± 3.9	8.22 ± 0.16	2	6.501 ± 1.189	10.278 ± 1.88	cypriano+04
Abell478	0.0881	48.8 ± 4.7	7.96 ± 0.27	2	9.168 ± 2.452	13.857 ± 3.707	okabe+14b
Abell2142	0.0904	64.3 ± 3.5	10.04 ± 0.26	2	8.777 ± 1.476	12.457 ± 2.095	umetsu+09
Abell2244	0.0989	27.2 ± 2.7	5.37 ± 0.12	2	3.157 ± 2.391	4.678 ± 3.543	kubo+09
Abell2034	0.113	28.8 ± 2.7	7.15 ± 0.32	1	5.169 ± 3.1	8.086 ± 4.849	okabe&08
Abell2204	0.1511	53 ± 5.2	8.55 ± 0.58	2	16.051 ± 2.963	23.197 ± 4.283	applegate+14
Abell2218	0.171	33.5 ± 3.2	6.97 ± 0.37	1	5.108 ± 1.358	7.697 ± 2.047	mahdavi+13
Abell1914	0.1712	54.4 ± 5.5	9.48 ± 0.49	1	5.6 ± 1.009	8.451 ± 1.523	mahdavi+13
Abell665	0.1818	56.5 ± 5.2	8.03 ± 0.24	1	8.186 ± 4.621	12.461 ± 7.035	pedersen&07
Abell520	0.203	64.1 ± 2	7.23 ± 0.23	3	5.516 ± 1.272	8.343 ± 1.925	mahdavi+13
Abell963	0.206	34.7 ± 1.5	6.08 ± 0.3	3	4.583 ± 1.637	6.623 ± 2.365	applegate+14
Abell1423	0.213	39.7 ± 2.4	5.75 ± 0.59	3	11.568 ± 5.823	16.282 ± 8.196	dahle06
Abell773	0.217	47.7 ± 1.5	7.37 ± 0.45	3	16.757 ± 7.814	25.985 ± 12.118	pedersen&07
Abell2261	0.224	56.3 ± 2.3	6.1 ± 0.32	3	14.663 ± 2.394	21.246 ± 4.09	umetsu+14
Abell1682	0.226	49.6 ± 6.1	7.01 ± 2.14	3	4.014 ± 2.307	6.048 ± 3.476	pedersen&07
Abell1763	0.2279	72.9 ± 3.9	6.32 ± 0.4	3	9.989 ± 2.516	15.329 ± 3.86	mahdavi+13
Abell2219	0.2281	95.8 ± 5.3	10.9 ± 0.53	3	11.729 ± 1.852	16.951 ± 2.677	applegate+14
Abell2111	0.229	36.1 ± 2.2	6.51 ± 0.72	3	4.498 ± 1.491	6.795 ± 2.251	mahdavi+13
Abell267	0.23	33.6 ± 1.6	7.13 ± 0.71	3	5.245 ± 1.523	7.948 ± 2.308	mahdavi+13
Abell2390	0.2329	86.9 ± 2.9	10.28 ± 0.38	3	11.183 ± 2.396	16.162 ± 3.463	applegate+14
Abell1835	0.2528	67.3 ± 2.3	9.0 ± 0.25	3	15.51 ± 4.503	22.417 ± 6.508	applegate+14
Abell68	0.2546	44.2 ± 2.7	7.56 ± 0.97	3	9.171 ± 1.587	13.254 ± 2.294	applegate+14
Abell697	0.282	89.5 ± 5	10.93 ± 1.11	3	9.531 ± 1.303	14.694 ± 2.009	mahdavi+13
Abell781	0.2984	51 ± 3.2	7.55 ± 1.03	3	9.655 ± 4.393	13.78 ± 6.27	dahle06
Abell85	0.0557	30.4 ± 2	6.45 ± 0.1	2	4.579 ± 1.245	7.24 ± 1.968	cypriano+04
Abell2597	0.0852	12.9 ± 1.3	3.58 ± 0.07	1	2.803 ± 1.047	4.432 ± 1.656	cypriano+04
Abell1689	0.1832	57.2 ± 5.7	9.15 ± 0.35	1	12.614 ± 1.671	16.843 ± 2.429	umetsu+11
Abell209	0.206	58 ± 2.2	8.23 ± 0.66	3	11.573 ± 1.796	17.559 ± 2.993	umetsu+14
Abell521	0.2475	58 ± 2.1	6.21 ± 0.28	3	8.082 ± 1.94	11.68 ± 2.803	applegate+14
Abell2537	0.2966	38.7 ± 2.9	7.63 ± 0.86	3	7.068 ± 1.113	10.841 ± 1.707	mahdavi+13
MACSJ1115.8+0129	0.355	54.3 ± 2.5	9.2 ± 0.98	3	9.259 ± 1.991	15.531 ± 3.385	umetsu+14
MACSJ0949.8+1708	0.384	62.3 ± 4.1	8.92 ± 1.83	3	8.874 ± 4.075	12.825 ± 5.889	applegate+14
MACSJ1731.6+2252	0.389	74.2 ± 4.3	5.87 ± 0.61	3	22.817 ± 4.087	32.977 ± 5.906	applegate+14
MACSJ2211.7-0349	0.396	101.5 ± 6.3	13.97 ± 2.74	3	13.447 ± 2.881	19.434 ± 4.164	applegate+14
MACSJ0429.6-0253	0.399	39.1 ± 2.5	8.33 ± 1.58	3	6.765 ± 1.89	9.351 ± 2.984	umetsu+14
MACSJ1206.2-0847	0.439	105.5 ± 6.4	10.71 ± 1.29	3	10.542 ± 2.089	15.813 ± 3.58	umetsu+14
MACSJ0417.5-1154	0.443	152.9 ± 9.4	9.49 ± 1.12	3	21.176 ± 3.97	30.605 ± 5.738	applegate+14
MACSJ2243.3-0935	0.447	115.6 ± 6.7	8.24 ± 0.92	3	20.294 ± 3.865	29.33 ± 5.587	applegate+14
RXJ0439.0+0715	0.2443	42.2 ± 1.6	6.59 ± 0.45	3	9.753 ± 4.955	13.792 ± 7.006	dahle06
Zwicky5247	0.229	37.4 ± 2.4	5.31 ± 1.07	3	2.472 ± 2.042	3.49 ± 2.883	dahle06
Zwicky2089	0.2347	17 ± 1.3	6.55 ± 1.47	3	3.55 ± 2.965	5.02 ± 4.193	dahle06
Zwicky3146	0.2906	58.2 ± 2.6	8.38 ± 0.44	3	12.071 ± 5.271	18.72 ± 8.175	pedersen&07

z, L_X and T_X are redshift, core-excised X-ray temperature and core-excised soft band luminosity of the cluster from Mantz et al. (2010). kT ref. gives the reference for temperatures in Mantz et al. (2010), (1) are *ASCA* temperatures from Horner (2001), 2 and 3 are *Chandra* temperatures from Vikhlinin et al. (2009) and Mantz et al. (2010). M_{500}, M_{200} and author code the spherical overdensity masses with respect to the critical density and author code fields in the LC^2 catalogue of Sereno (2014). Author code applegate+14 points to Applegate et al. (2014), cypriano+04 to Cypriano et al. (2004), dahle06 to Dahle (2006), kubo+09 to Kubo et al. (2009), mahdavi+13 to Mahdavi et al. (2013), okabe&08 to Okabe & Umetsu (2008), okabe+14b to Okabe et al. (2014), pedersen&07 to Pedersen & Dahle (2007), umetsu+09 to Umetsu et al. (2009), umetsu+11 to Umetsu et al. (2011) and umetsu+14 to Umetsu et al. (2014).

Table C2. The Eddington bias corrections for the literature high-mass sample.

Name	$\frac{d\alpha(ln(M))}{d\ln(M)}$	$M_{\rm rat}$	$T_{\rm X, rat}$	$L_{\rm X, rat}$
Abell2029	1.879	0.845	0.930	0.595
Abell478	2.244	0.817	0.916	0.538
Abell2142	2.116	0.827	0.921	0.561
Abell2244	1.234	0.895	0.953	0.710
Abell2034	1.689	0.859	0.935	0.627
Abell2204	3.163	0.753	0.879	0.417
Abell2218	1.725	0.856	0.933	0.621
Abell1914	1.818	0.849	0.930	0.604
Abell665	2.282	0.815	0.915	0.533
Abell520	1.854	0.846	0.930	0.603
Abell963	1.635	0.863	0.937	0.640
Abell1423	2.724	0.783	0.888	0.474
Abell773	3.555	0.727	0.867	0.380
Abell2261	3.193	0.751	0.881	0.419
Abell1682	1.582	0.867	0.868	0.643
Abell1763	2.665	0.787	0.898	0.483
Abell2219	2.821	0.776	0.894	0.462
Abell2111	1.691	0.859	0.927	0.629
Abell267	1.847	0.847	0.923	0.604
Abell2390	2.757	0.781	0.898	0.472
Abell1835	3.369	0.739	0.878	0.399
Abell68	2.511	0.798	0.889	0.503
Abell697	2.723	0.783	0.888	0.475
Abell781	2.663	0.787	0.880	0.482
Abell85	1.516	0.872	0.943	0.660
Abell2597	1.185	0.899	0.955	0.720
Abell1689	2.709	0.784	0.899	0.472
Abell209	2.826	0.776	0.889	0.463
Abell521	2.325	0.811	0.912	0.531
Abell2537	2.325	0.811	0.901	0.528
MACSJ1115.8+0129	2.987	0.765	0.877	0.443
MACSJ0949.8+1708	2.751	0.781	0.847	0.471
MACSJ1731.6+2252	4.651	0.659	0.816	0.280
MACSJ2211.7-0349	3.500	0.730	0.815	0.384
MACSJ0429.6-0253	2.337	0.811	0.875	0.527
MACSJ1206.2-0847	3.236	0.748	0.863	0.412
MACSJ0417.5-1154	4.661	0.658	0.809	0.279
MACSJ2243.3-0935	4.569	0.664	0.816	0.287
RXJ0439.0+0715	2.546	0.795	0.901	0.500
Zwicky5247	1.176	0.899	0.932	0.724
Zwicky2089	1.439	0.879	0.911	0.673
Zwicky3146	3.142	0.754	0.883	0.424

$\frac{d\alpha(ln(M))}{d\ln(M)}$ is the slope of the mass function, $M_{\rm rat}$, $T_{\rm X,rat}$ and $L_{\rm X,rat}$ are the ratio of the Eddington BC mass, temperature and luminosity to the uncorrected values.

[1]*Department of Physics, University of Helsinki, PO Box 64, FI-00014 Helsinki, Finland*

[2]*Helsinki Institute of Physics, University of Helsinki, PO Box 64, FI-00014 Helsinki, Finland*

[3]*Leiden Observatory, Leiden University, PO Box 9513, NL-2300 RA Leiden, the Netherlands*

[4]*Argelander-Institut für Astronomie, Auf dem Hügel 71, D-53121 Bonn, Germany*

[5]*Max-Planck-Institut für Extraterrestrische Physik, GiessenbachstraÃe, D-85740 Garching, Germany*

[6]*Scottish Universities Physics Alliance, Institute for Astronomy, University of Edinburgh, Royal Observatory, Blackford Hill, Edinburgh EH9 3HJ, UK*

[7]*Department of Physics and Astronomy, University of British Columbia, 6224 Agricultural Road, Vancouver, BC V6T 1Z1, Canada*

[8]*Mullard Space Science Laboratory, University College London, Holmbury St Mary, Dorking, Surrey RH5 6NT, UK*

[9]*Department of Physics and Astronomy, San Francisco State University, 1600 Holloway Avenue, San Francisco, CA 94132, USA*

[10]*Sorbonne UniversiteÌs, UPMC Univ Paris 06, UMR 7095, Institut dAstrophysique de Paris, F-75014 Paris, France*

[11]*CNRS, UMR 7095, Institut dAstrophysique de Paris, F-75014 Paris, France*

[12]*Department of Physics, Oxford University, Keble Road, Oxford OX1 3RH, UK*

[13]*Astronomical Observatory of the University of Geneva, ch. dEcogia 16, CH-1290 Versoix, Switzerland*

[14]*Institute of Astronomy and Astrophysics, Academia Sinica, PO Box 23-141, Taipei 10617, Taiwan*

[15]*Steward Observatory, University of Arizona, 933 North Cherry Avenue, Tucson, AZ 85721, USA*

[16]*Shanghai Key Lab for Astrophysics, Shanghai Normal University, 100 Guilin Road, 200234 Shanghai, China*

[17]*Department of Physics and Astronomy, University of Waterloo, 200 University Avenue West, Waterloo, ON N2L 3G1, Canada*

[18]*Perimeter Institute for Theoretical Physics, 31 Caroline Street N, Waterloo, ON N2L 1Y5, Canada*

[19]*Laboratoire d'Astrophysique de Marseille, CNRS-Université, Ple de l'Etoile Site de Château-Gombert 38, rue Frédéric Joliot-Curie, F-1338 Marseille, France*

[20]*Laboratoire dAstrophysique EPFL, Observatoire de Sauverny, CH-1290 Versoix, Switzerland*

[21]*Department of Physics and Astronomy, University College London, Gower Street, London WC1E 6BT, UK*

[22]*California Institute of Technology, 1200 E California Boulevard, Pasadena, CA 91125, USA*

[23]*Kavli Institute for Particle Astrophysics and Cosmology, Stanford University, 382 Via Pueblo Mall, Stanford, CA 94305-4060, USA*

[24]*National Astronomical Observatory of Japan 2-21-1 Osawa, Mitaka, Tokyo 181-8588, Japan*

This paper has been typeset from a TEX/LATEX file prepared by the author.